Apatite-glaucony association in the Ediacaran Doushantuo Formation, South China and implications for marine redox conditions

Majed Algabri [a], Zhenbing She [a, b], Liangxuan Jiao [a], Dominic Papineau [b, c, d, e], Guoqing Wang [a], Chao Zhang [f], Dongjie Tang [g], Guang Ouyang [a, b], Yaguan Zhang [a], Guoyong Chen [h], Chao Li [b]

[a] School of Earth Sciences, China University of Geosciences, Wuhan 430074, China

[b] State Key Laboratory of Biogeology and Environmental Geology, China University of Geosciences, Wuhan 430074, China

[c] London Centre for Nanotechnology, 17-19 Gordon Street, University College London, London WC1H 0AH, UK

[d] Department of Earth Sciences, University College London, London WC1E 6BT, UK

[e] Centre for Planetary Science, University College London and Birkbeck College, London WC1E 6BT, UK

[f] Institute of Mineralogy, Leibniz University Hannover, Hannover 30167, Germany

[g] Institute of Earth Sciences, China University of Geosciences, Beijing 100083, China

[e] Guizhou Bureau of Geology and Mineral Exploration and Development, Guiyang 550000, China

Abstract

Major phosphogenic events took place in the late Paleoproterozoic and the Ediacaran, both of which followed an episode of atmospheric oxygenation. These apparent coincidences have led to suggestions that the Precambrian phosphorus cycle was partly regulated by oceanic redox conditions, although direct evidence is lacking. In this paper, we report the discovery of glaucony in drill cores from the phosphorite-rich Ediacaran Doushantuo Formation at Weng'an, South China, which provides new insights into redox conditions and geochemical cycles during the deposition and early diagenesis of the lower Doushantuo Formation. The presence of flaser and lenticular bedding in the sandstones suggests deposition in a tidally-influenced shallow water environment. Apatite is present as millimeter-scale flasers in sandstones, but more commonly as intraclastic grains. Glaucony typically occurs as interstitial aggregates cementing and replacing detrital minerals and phosphatic grains, with an upsection decrease in abundance. The Doushantuo glauconies have consistently high K_2O (7.6 – 9.6 wt%). In particular, phosphorite-hosted

glaucony has generally higher total iron (TFe_2O_3) than sandstone-hosted glaucony, consistent with Al^{3+} - Fe^{3+} substitution in the octahedral site, as supported by Raman peaks slightly shifted towards lower wavenumbers for higher Fe content. A decrease in detrital input probably resulted in limited Al availability during early diagenesis, which in turn led to the waning of glaucony upsection. The phosphate grains do not show any negative Ce anomalies, consistent with precipitation of authigenic apatite in suboxic environments with insignificant preferential remobilisation of Ce during deposition and early diagenesis. REE + Y features show variable diagenetic REE enrichment in phosphorites, but identical concave-down patterns. The wide occurrence of glaucony cement further documents the presence of a generally suboxic early diagenetic environment on the seafloor, which was in active exchange with bottom seawater. Slight fluctuations of redox states in the porewater and bottom water would have promoted the cycling of Fe, enrichment of phosphate and REE, and extensive glaucony authigenesis. Therefore, the glaucony-bearing phosphorites in the Doushantuo Formation are a direct result of Fe-redox driven diagenesis. Apatite-glaucony association likely forms in suboxic environments and is considered as a useful mineralogical proxy for paleoredox conditions on the Precambrian ocean floors.

Keywords: Mineralogy; diagenesis; rare earth element; phosphogenesis; glauconitization

1. Introduction

The distribution of major phosphate deposits in the Precambrian sedimentary record is restricted to the Paleoproterozoic era and the Ediacaran period, both of which witnessed similar types of global biogeochemical changes (Papineau, 2010). These fundamental changes have generally been related to oxygenation of the Earth' s atmosphere and oceans (Och and Shields-Zhou, 2012; Pufahl and Hiatt, 2012; Lyons et al., 2014). Recent studies have shown that Precambrian phosphorites mainly occur in peritidal environments, in contrast to Phanerozoic phosphorites that accumulated across the entire shelf (Nelson et al., 2010). These observations have led to the suggestion that Precambrian phosphogenesis is closely related to redox variations of paleo-seawater that regulated the cycling of phosphorus through the adsorption and reductive desorption of phosphate on Fe-

oxyhydroxides (Nelson et al., 2010; Pufahl and Hiatt, 2012; Hiatt et al., 2015; She et al., 2014; Cui et al., 2016; Zhang et al., 2019).

The Doushantuo Formation (ca. 635-551 Ma) in South China is an important site for constraining the Ediacaran ocean redox conditions and biological evolution (Xiao et al.,1998; Bailey et al., 2007; McFadden et al., 2008; Li et al.,2010; Shen et al., 2010; Sahoo et al., 2012). Redox sensitive trace element (RSTE) and Fe speciation data suggest that Ediacaran seawater along the South China Craton margin featured redox stratification, with an oxic surface ocean that was underlain by a thin ferruginous layer, a metastable wedge of euxinic water resting on the open shelf, and a deep ferruginous ocean (e.g., Li et al., 2010; Wang et al., 2012; Muscente et al., 2015; Fan et al., 2018). More recently, studies have shown that Ediacaran marine redox chemistry was highly heterogeneous, even at the kilometer-scale (e.g., Li et al., 2015). While Fe speciation and RSTEs data can provide relatively accurate information on marine bottom-water redox conditions suitable for silicilastic rocks (Tribovillard et al., 2006; Lyons and Severmann, 2006), most of these proxies have not been applied to phosphorites. The Doushantuo Formation at the shallow water Weng'an section is largely composed of carbonate and phosphorite and the redox conditions during phosphogenesis remain unclear.

Fe-bearing authigenic minerals have the potential to record the chemistry and redox conditions of the pore water and probably of the bottom water. Glauconite [(K, Na, Ca) (Fe, Al, Mg, Mn)$_2$ (Si, Al)$_4$ O$_{10}$ (OH)$_2$] is a K- and Fe-rich phyllosilicate mineral of dioctahedral mica group with 2:1 + interlayer ion structures, while the term glaucony is used to represent a series of green clay minerals with a wide range of chemical/mineralogical compositions including glauconitic mica, glauconitic smectite, and ferric illite (Odin and Létolle, 1980; Odin and Matter, 1981; Meunier and El Albani, 2007; Banerjee et al., 2015, 2016b). Glaucony is known to occur in marine sedimentary rocks ranging in age from Precambrian to Holocene, where it commonly occurs in green clay aggregates usually 60 -1000 μm in diameter (Odin and Matter, 1981; Dasgupta at al.,1990; Chafetz and Reid, 2000; Lee et al., 2002; El Albani et al., 2005; Meunier and El Albani, 2007; Amorosi et al., 2007; Banerjee et al., 2015; 2016b). Although glauconitic minerals are generally considered to be an effective indicator of low sedimentation rate in marine

environments and is commonly associated with transgression (Odin and Matter, 1981; Amorosi, 1997; Harris and Whiting, 2000; Giresse and Wiewio, 2001; Chattoraj et al., 2009; Banerjee et al., 2008; 2015; 2016b), they have also been reported from regressive sediments with a normal sedimentation rate (Chafetz and Reid, 2000). In the modern ocean, glaucony forms on the continental shelves at a depth range between 50 and 500 m and is most abundant between the upper slope and the outer shelf at depths around 200-300 m (Odin and Matter, 1981). Likewise, Phanerozoic glaucony is interpreted to have formed in middle to outer shelf depositional conditions (Banerjee et al., 2016b). Precambrian glaucony, however, is thought to have occurred in shallow marine depositional conditions, mostly within the shoreface region (Banerjee et al., 2016b), and is rarely preserved probably due to its alteration or metamorphic recrystallization into other phyllosilicates.

Apatite-glaucony associations have been observed in modern offshore environments associated with significant upwelling, which also cause phosphatization, such as off the coast of Peru, Chile, California, South Africa, Namibia, Spain, northwest Africa, east Australia, and west India (Burnett, 1980; Mullins and Rasch, 1985; Odin and Lamboy, 1988; Rao et al., 1993; Wigley and Compton, 2007; Banerjee et al., 2016a; Föllmi, 2016) and in Phanerozoic successions as old as the early Cambrian (Braiser, 1980). In this paper, we report on the discovery of apatite-glaucony association in the lower Doushantuo Formation at Weng'an, South China. Drill core samples from three boreholes near Weng'an are studied and complemented by analyses of the sedimentology, mineralogy, and geochemistry of glaucony and apatite to provide new insights into the redox conditions during the deposition and early diagenesis of the Doushantuo Formation.

2. Geological setting

The Doushantuo Formation is a carbonate-black shale sequence that is widespread in South China (Jiang et al., 2011). It is economically important because of the discovery of major phosphorite deposits that account for 51% of the total phosphorus reserves in China according to an early estimate (Fig.1a; Ye et al., 1989). According to an earlier paleogeographic reconstruction, the Doushantuo Formation in the Yangtze platform was deposited on a rimmed carbonate shelf with Weng'an located on the shelf margin (Fig.1a; Jiang et al., 2011). In the Weng'an and nearby Kaiyang areas, however, the common

occurrence of terrigenous clasts, cross stratification and wave ripples in the Doushantuo Formation is more consistent with deposition in a more proximal, mixed clastic-chemical costal environment (Chen et al., 2015; Zhang et al., 2019). The current study is focused on the Doushantuo Formation in drillholes close to the northern margin of the Baiyan anticline (Fig. 1b). In this area, the Neoproterozoic Qingshuijiang Formation occurs along the axis of the anticlines while the Cambrian System is exposed on the limbs, with the Ediacaran Doushantuo and Dengying Formations sandwiched in between.

The Doushantuo Formation was first typified in the Yangtze Gorges area where it overlies Cryogenian diamictite of the Nantuo Formation and underlies the upper Ediacaran Dengying Formation (Xiao et al., 2014). Lithostratigraphically, the Doushantuo Formation is subdivided into four members, including the cap dolostone unit (Member I) at the base, followed upsection by interbeded dolostone and black shale (Member II), carbonate (Member III), and black shale (Member IV) at the top (e.g., Zhou et al., 2007). At Weng'an, the stratigraphy of the Doushantuo Formation is broadly correlated with its counterpart in the Yangtze Gorges area according to the underlying Cryogenian diamictite and the overlying dolostones of the Dengying Formation, but a one-to-one correlation to the four members is not straightforward. Instead, the Doushantuo Formation is subdivided into five lithological units (Fig. 1c). It consists of, in ascending order, a basal cap dolostone unit (Unit 1), a thin-bedded, peloidal phosphorite unit (Unit 2, the 'lower phosphorite'), a massive dolostone unit (Unit 3) with a prominent karstification surface on top, an intraclastic phosphorite unit (Unit 4, the 'upper phosphorite'), which is further divided into the lower Unit 4A (black facies) and the upper Unit 4B (grey facies), and a phosphatic dolostone unit (Unit 5) probably containing an additional exposure surface (Xiao et al., 2014).

The depositional age of Doushantuo Formation in the Yangtze Gorges area has been constrained as 635-551 Ma (Condon et al., 2005). For the Weng'an counterpart, previous studies have yielded Pb-Pb isochron ages of 572 ± 36 Ma for Unit 4A (Chen et al., 2009), 599 ± 4 Ma for Unit 4B (Barfod et al., 2002) and 576 ± 14 Ma (Chen et al., 2004). Recently, a SIMS zircon U–Pb age of 609 ± 5 Ma was reported from a tuff layer which lies immediately above the upper phosphorite unit (correlated with unit 4 at Weng'an) in

Yichang, 600 km to the northeast of Weng'an (Zhou et al., 2017). The new age data suggests that the major phosphorite beds were likely deposited between 635 and 609 Ma.

In this study, stratigraphic sections of three boreholes (Zk1202, Zk208, Zk115; GPS coordinates: 27°4′29.2″N / 107°24′19.8″E, 27°04′56.7″N / 107°24′48.9″E, 27°04′45.4″N / 107°24′24.5″E) in the Weng'an area are studied (Fig. 1b). In these drill cores, the lithology of Units 1 to 5 vary (Fig. 1c), and their thicknesses are 1.4–3.8 m, 18.5–24.3 m, 0.6–4.4 m, 0.7–5.0 m and ~3.83 m, respectively. Moreover, the basal unit is dominated by glaucony-bearing siliciclastic sediments rather than dolostone. Such a basal siliciclastic unit is considered synchronous with widespread cap carbonate deposition (Zhang et al., 2019). The glaucony-bearing sandstones are generally characterized by sandstone layers intercalated with flasers of mudrock or phosphorite (Fig. 2a), suggesting deposition in a tidal-influenced environment. In Zk1202 and Zk208, glaucony is also present in the lower phosphorite unit (Unit 2), although it shows a generally decreasing trend in abundance (Fig. 1c). The base of the Doushantuo Formation features glauconitic sandstones, consistent with deposition in coastal environments as a result of marine transgression following the Marinoan glaciation (Zhang et al., 2019). Upsection, the transition to bedded phosphorite and dolostone in Units 2-5 points to a decrease of terrigenous input and an increase of authigenic phosphate and carbonate, consistent with a transgression into a deeper environment. We focus on the glaucony-bearing Units 1 and 2, which are termed as the lower Doushantuo Formation in this study.

3. Material and methods

3.1. Samples

Ninety-nine samples were collected from the three drill cores (Zk1202, Zk208 and Zk115) in Weng'an (Fig. 1b). The samples were cut into chips and only the fresh parts are used for thin section and mineralogical/geochemical analyses. Prepared thin sections and rock slabs were further polished with 500 nm Al_2O_3 and cleaned with deionized water prior to analyses with light microscopy, scanning electron microscopy, Raman micro-spectroscopy, energy dispersive X-ray spectrometry and laser ablation inductively coupled plasma mass spectrometry. For x-ray diffractometry and electron probe microanalysis, a

selection of samples was cleaned, dried and powdered (~200 mesh) in an agate mortar that was carefully washed and dried before the grinding. Glaucony-rich grains were separated from the samples using a combination of magnetic, electrostatic and handpicking techniques. Care was taken to avoid cross-contamination in each step.

3.2. Optical microscopy

Petrographic studies were carried out on polished thin sections and rock slabs using a Zeiss Axio Scope.A1 microscope attached to an Axio MRe5 camera, at School of Earth Seicnces, China University of Geosciences (Wuhan). Mineralogy and microfabrics were documented with 5×, 10×, 20×, 50× and 100× objectives under the transmitted light and reflected light modes, with targets of interests mapped for further *in situ* microanalysis.

3.3. Scanning electron microscopy and energy dispersive X-ray spectrometry

Scanning electron microscopy (SEM) was carried out on polished thin sections using a Zeiss Supra 55 field- emission SEM (FE-SEM) under 20 kV accelerating voltage, at the State Key Laboratory of Biogeology and Environmental Geology, China University of Geosciences (Beijing). A backscattered electron (BSE) detector was used to characterize compositional difference. Samples were coated with ~10-nm-thick platinum for electric conduction prior to analysis.

Quantitative element analysis of micron-sized spots was conducted using an Oxford energy dispersive X-ray spectrometer (EDS) attached to the Zeiss Supra 55 FE-SEM, operated at an acceleration voltage of 20 kV with a working distance of 15 mm, specimen current of 200 nA, and a beam diameter of ~1 μm. Minerals as well as synthetic phases (MINM25-53) were used as standards. Duplicate analyses of individual points show analytical analytical error less than 2%.

3.4. Raman micro-spectroscopy

Raman micro-spectroscopy was conducted at the State Key Laboratory of Biogeology and Environmental Geology, China University of Geosciences (Wuhan) using a WITec α 300 Confocal Raman system coupled with a Peltier cooled EMCCD detector. Laser

excitation at 532 nm with output power between 3 to 10 mW was used. Spectra were obtained using a 100 × (N.A. = 0.9) magnification objectives with a 50 μm diameter optic fiber. A grating of 600 g/mm was used, yielding a spectral resolution of ~4 cm^{-1}. Considering the weak Raman scattered signal of glaucony, presumably due to the fine crystallinity, we set the integration time for each spectrum from 30 to 80 s, and the number of accumulations from 2 to 5, in order to achieve a sufficiently high signal-to-noise ratio. The Raman spectra were collected at confocal depths of at least one μm below the thin section surface. The WITec Project Five 5.1 Plus software was used to process for all Raman spectra. The spectra were processed with a background subtraction polynomial fit, typically of the order of 4-6.

3.5. Electron probe microanalysis

Glaucony separates were mounted in epoxy resin, polished and coated with a thin carbon layer with a thickness of ca. 200 Å. Major element analyses were performed with a Cameca SX100 electron microprobe equipped with five spectrometers and "PeakSight" operation software at the Institute of Mineralogy, Leibniz University Hannover, Germany. The major elements (including total Fe expressed as TFe_2O_3) were measured using calibration standards of synthetic oxides (Fe_2O_3, Al_2O_3, Cr_2O_3, Mn_3O_4, MgO and TiO_2), natural wollastonite (for Si and Ca), orthoclase (for K), and jadeite (for Na). The measurements were conducted with an accelerating voltage of 15 kV, a beam current of 15 nA and a defocused beam (diameter 5 μm). The quantification of all major elements was based on Kα intensities, and raw data were corrected using the standard PAP procedure (Pouchou and Pichoir, 1991).

3.6. X-ray diffractometry

The mineralogical composition of a glaucony-enriched separate (ZK1202-04) was determined by the X-ray diffraction (XRD) technique using a Dandong TD-3500 advance diffractometer equipped with nickel filtered CuKα radiation (35 kV, 25 mA) at State Key Laboratory of Biogeology and Environmental Geology, China University of Geosciences (Wuhan). The air-dried, powdered sample was scanned from 3° to 65° with a step size of 0.02° 2θ and a scan speed of 0.25°/min.

3.7. Laser ablation inductively coupled plasma mass spectrometry

Major and trace element concentrations in apatite grains were measured by laser ablation inductively coupled plasma mass spectrometry (LA-ICP-MS) at Wuhan Sample Solution Analytical Technology Co., Ltd. Prior to analysis, target spots on apatite grains devoid of veins and secondary cement were selected and mapped in polished slabs (with a last 0.5 μm alumina polish step) under the reflected light. In total, 68 spots were analyzed *in situ* on 17 polished slabs. Laser sampling was performed using a GeolasPro laser ablation system that consists of a MicroLas optical system and a COMPexPro 102 ArF excimer laser (wavelength 193 nm). A spot size of 32 μm was used for all analyses, with laser repetition rate of 5 Hz and energy density of ~5.5 j/cm^2. Ion-signal intensities were acquired with an Agilent 7700e ICP-MS. Helium was used as a carrier gas and Argon was used as the make-up gas and mixed with the carrier gas via a T-connector before entering the ICP. Each analysis incorporated a background acquisition of approximately 20-30 s (gas blank) followed by 50 s of data acquisition from the sample. Element contents were calibrated against multiple-reference materials (BCR-2G, BIR-1G and BHVO-2G) without applying internal standardization (Liu et al., 2008). An Excel-based software ICPMSDataCal was used to perform off-line selection and integration of background and analyzed signals, time-drift correction and quantitative calibration for major and trace element analyses (Liu et al., 2010). The analytical precision (RSD) is better than 10% for major and trace elements, whereas the accuracy is better than 10% except for Pr, Gd, Ho, and Tm (better than 15 %).

4. Results

4.1. Petrography and occurrences of phosphate and glaucony

A compilation of phosphorite and glaucony occurrences in the Doushantuo Formation shows that phosphorite deposits are mainly distributed in coastal environments and shallower parts of the shelf, whereas glaucony is restricted to coastal environments (Table 1, Fig. 1a). Apatite-glaucony association is only reported from central Guizhou, including Weng'an and Kaiyang.

At Weng'an, the lower Doushantuo Formation mainly consists of glaucony-bearing sandstone in the lower part and granular phosphorite in the upper part (Fig. 1c, Fig. 2). The former may contain a dolostone interbed. The lower Doushantuo rocks contain variable amounts of terrigenous grains, e.g., detrital quartz, feldspar and muscovite, and intraclastic grains (Fig. 2c-n). In the sandstones, dark brown, millimeter- to submillimeter- scale phosphatic flasers were observed and can be locally abundant (Fig. 2a, c-d). They exhibit an anastomosing microstructure and are composed of organic-rich, cryptocrystalline apatite mixed with micrometer-sized detrital particles and sulfides (Fig. 2d). The detrital minerals commonly occur as angular to subangular grains that are 100 to 300 μm in diameter. The intraclasts are dominated by phosphate (francolite) and glauconitized phosphate (Gl-Ap) grains, which account for 20 to 30% of the total clasts in glauconitic sandstones and up to 100% in granular phosphorites. They occur as elongate to elliptical, angular to sub-rounded grains ranging from 200 to 750 μm in diameter (Fig. 2k-n). The grains contain variable amounts of glaucony and apatite, giving rise to their greenish to brownish colors (Fig. 2d-e, k-n). Other than that, in Gl-Ap grains, glaucony is mainly present as interstitial cement in the sandstones and phosphorites (Fig. 2d-g, i-k). Two types of glaucony have been distinguished according to their host lithology.

Type 1 Sandstone-hosted glaucony. It mainly occurs as interstitial authigenic cement in sandstones (Fig. 2d-g, i-k; 3a-b). Glaucony accounts for up to 30% by volume. Partial replacement of detrital quartz (Fig. 2f; 3a), K-feldspar (Fig. 2h; 3b) and muscovite (Fig. 2i-j) by glaucony was observed, suggesting that these detrital grains acted as the original substrate for the growth of glaucony. In the BSE images, gray, porous aggregates of glaucony are distinguishable from dark gray, smooth quartz grains (Fig. 3a-b). EDS analyses confirm that these porous aggregates are glaucony that contains K, Si, Al, Mg and Fe (Fig. 3g). They also document the presence of K-feldspar and that the interstitial cement is dominated by glaucony that contains Si, K, Al, Mg and small amounts of Fe (Fig. 3g).

Type 2 Phosphorite-hosted glaucony. This type occurs as bluish to greenish patches in Ap-Gl grains (Fig. 2l-n; 3e) or as interstitial cement (Fig. 2k-l; 3c, e). The grains typically consist of a mixture of glaucony, apatite and sulfide (Fig. 2l-n), occasionally with barite (Fig. 3f). They have distinct physical boundaries with the surrounding phosphatic grains.

In the glaucony-hosting phosphorite, glaucony accounts for about 15% of the samples by volume. High magnification secondary electron images (Fig. 3d) further show a distinct lamellar and platy habit, typical of phyllosilicate minerals, including glaucony. EDS spot analyses confirm the presence of K, Si, Al, Mg and Fe in type 2 glaucony (Fig. 3g). EDS elemental maps show the coexistence of Si, Al, K and Fe in the glaucony, roughly complementary to the distribution of P (Fig. 3h). These observations demonstrate the close association of apatite and glaucony at the micrometer scale.

Sulfides, mostly pyrite, are also common in the samples. They occur as anhedral to euhedral grains with variable sizes of 10 – 200 μm (Fig. 2d-e, g, k-n; 3f). In particular, micrometer-sized sulfide crystals are ubiquitously present with high abundance in the phosphate-glaucony grains and glaucony cement (Fig. 3l-n), making it impossible to obtain pure glaucony separate with standard separation techniques. Sulfides are relatively more abundant in the phosphorites than in the sandstones.

4.2. Mineralogical characterization by XRD

The X-ray diffraction spectrum of the glauconitic sandstone shows that the bulk sample is composed of glauconite, illite, quartz and dolomite (Fig. 4). The sample exhibits characteristic peaks of glauconite characterized by basal reflection (001) at 10.20 Å, and two reflections (020) and (005) at 4.51 Å and 1.97Å, respectively (Fig. 4). In addition, the presence of basal reflections $(11\overline{2})$ at ca. 3.70 Å and (112) at 3.07 Å further distinguishes glaucony from illite. Instead, the reflections $(\overline{1}13)$ at 2.89 Å, the (032) at 2.79Å, the $(\overline{2}01)$ at 2.57 Å, and the (060) at 1.50 Å d-spacing confirm the presence of illite. This suggest the presence of illite as a mixture with glaucony, which is difficult to physically separate. The sample also exhibits quartz peaks of intense reflection (101) at 3.35 Å and evident reflections (100) at 4.25 Å, (003) at 1.81 Å and (211) at 1.54 Å. The presence of dolomite is also shown by the strong reflection (113) at 2.19 Å, and weak reflections (021), (202) and (116) at d-spacings between 2.06 and 1.78 Å (Fig. 4).

4.3. Raman spectra of glaucony and associated minerals

The Raman spectra of glaucony (Fig. 5) show characteristic bands in the range 100 – 800 cm $^{-1}$, and less well-defined peaks and broad bands in the range of H_2O/OH vibrational modes (3000 – 3700 cm^{-1}). Strong bands at 263 cm^{-1} and 701 cm^{-1} are observed for glaucony associated with phosphorite (type 2), and bands at 267 cm^{-1} and 705 cm^{-1} observed for glaucony associated with sandstone (type 1). Moreover, two weak, broad bands at 189 cm^{-1} and 443 cm^{-1} are present in all glaucony-bearing samples. The coexistence of the apatite peak (964 cm^{-1}) and glaucony peaks in the apatite target attests to the close spatial association of these two phases. The presence of a less well-defined peak near 3615 cm^{-1} in type 1 (sandstone-hosted) glaucony documents the presence of hydroxyl group. In type 2 glaucony, however, only a few broad, weak bands occur in the 3200 – 3700 cm^{-1} region, which likely indicates the presence of structural H_2O in the mineral (Wang et al., 2015). In type 2 (phosphorite-hosted) glaucony and apatite grains, weak bands for organic matter are also observed at ca. 1355 cm^{-1} (disordered carbon) and 1592 cm^{-1} (graphitic carbon).

It has been shown that strong bands in the range of 600 – 750 cm^{-1} characterize the Si–O–Si vibrations of phyllosilicates, whereas the exact peak positions are related to properties of cations (Mg, Fe, Ca, Al, etc.) that occupy adjacent octahedral sites (Wang et al., 2015). The systematic downshifts of main Raman peaks (267 to 263 cm^{-1}, 705 to 701 cm^{-1}, Fig. 5) from type 1 glaucony to type 2 glaucony probably reflect compositional variability caused by substitution of cations (e.g., Fe^{3+} for Al^{3+}) at the octahedral site. It is also noted that no discernable peak at 540 – 550 cm^{-1}, which is commonly present in Raman spectra of Phanerozoic glauconite (Ospitali et al., 2008; Wang et al., 2015), is observed for the Doushantuo glaucony.

4.4. Major element composition and structural formula of glaucony

Major element composition of the two types for glaucony (sandstone-hosted, ZK1202-04, 05) and (phosphorite-hosted, ZK1202-10) determined by EPMA and EDS analyses are given in Tables 2 and 3 (55 analyses in total). The measured total Fe is expressed as TFe_2O_3

for the calculation of structural formula (Banerjee et al., 2015; Tang et al., 2017). The calculated structural composition of two types of glaucony in the Doushantuo Formation are also presented in Tables 2 and 3. All elemental determinations were made on an anion equivalent basis to the structural formulae per $O_{10}(OH)_2$.

The major element compositions of the Doushantuo glaucony are comparable to those of Phanerozoic glauconies (Fig. 6a). However, the K_2O content in the Doushantuo glaucony are higher, falling in a narrow range between 7.6 to 9.6 wt%, which is independent of the type of glaucony. The TFe_2O_3 content of the glaucony types varies considerably in the range of 1.1 to 8.1 wt% with the lowest value in type 1 (sandstone-hosted) glaucony (avg. 4.0 wt%) and the highest in type 2 (phosphorite-hosted) glaucony (avg. 6.8 wt%). However, there is no correlation between K_2O and TFe_2O_3, because the two types of glaucony have distinct TFe_2O_3 contents (Fig. 6a). The K_2O *vs.* TFe_2O_3 relationship of the studied glaucony is similar to those reported from other Precambrian sedimentary successions (Fig. 6a; Tang et al, 2017; Banerjee et al., 2008, 2015; Dasgupta et al., 1990; Deb and Fukuoka, 1998; Drits et al., 2010; Ivanovskaya et al., 2006; Guimaraes et al., 2000; Sarkar et al., 2014). The Al_2O_3 content of the glaucony varies from 14.0 to 29.5 wt% and is higher in type 1 glaucony (avg. 23.3 wt%) than in type 2 (avg. 18.1 wt%). The good negative correlation between Al^{3+} (octahedral) and Fe^{3+} (octahedral) ($r^2 = 0.88$, Fig. 6b) indicates predominant Al^{3+} - Fe^{3+} substitution in the octahedral site (Odin and Matter, 1981; Dasgupta et al., 1990; Banerjee et al., 2008, 2012a, 2012b). The MgO content increases from 2.7 – 5.4 wt% for type 1 to 5.6 – 9.0 wt% for type 2 (Tables 2-3). The SiO_2 content shows small variations among the two types of glaucony, with average SiO_2 increases from (avg. 56.7 wt%) for type 1 to (avg. 57.4 wt%) for type 2. Na_2O, CaO, MnO, Cr_2O_3 and P_2O_5 concentrations of the Doushantuo glaucony are negligible.

According to the Association Internationale Pour l'Étude des Argiles (AIPEA), glauconite is defined as a dioctahedral mica with tetrahedral Al^{3+} (or Fe^{3+}) usually greater than 0.2 atoms per formula unit and octahedral R^{3+} greater than 1.2 atoms (Bailey, 1980). In the octahedral site, Al^{3+} is the major cation, varying between 0.85 to 1.63 atoms per formula unit (avg. 1.32), whereas the total Fe^{3+} is comparatively low, varying between 0.03 and 0.23 (average 0.13) atoms per formula unit. The octahedral R^{3+} of the Doushantuo

glaucony varies from 1.08 and 1.66 atoms, with an average of 1.45 atoms per formula unit, Mg^{2+} has an average of 0.57 atoms per formula unit (Tables 2-3), higher than most of the reported values (Jarrar et al., 2000; Banerjee et al., 2015; Tang et al., 2017). The average Si^{4+} and Al^{3+} contents in the tetrahedral sites are 3.76 and 0.33 atoms per formula unit, respectively, indicating low Al^{3+}- Si^{4+} substitution at the tetrahedral sites in the Doushantuo glaucony. Meunier and El Albani (2007) proposed a cross plot of M^+ / 4Si (M^+ = interlayered cations) vs. (Fe octahedral) / Sum Oct. (sum of octahedral charge) to characterize the compositional ranges of minerals forming the solid solution series of glauconite, Fe-illite and Fe-Al smectite. Most of the analyzed Doushantuo glaucony falls in the field of glaucony and Fe-illite (Fig. 6c).

4.5. Rare earth element composition of phosphorite

REE+Y concentrations of 68 spots analyzed on 17 granular phosphorite slabs (3-4 spots for each slab) are presented in Table 4. The average composition of each sample is also calculated after data screening using the criteria of $Al_2O_3 < 0.5\%$ and $P_2O_5 > 30\%$. *In situ* analysis with LA-ICP-MS allows site-specific measurements on REE-rich apatite granules and specifically avoids other REE-bearing phases such as carbonate and silica minerals. Patterns normalized to Post-Archean Australian Shale (PAAS; McLennan, 1989) are presented for the average composition of each sample (Fig. 7a). Because relative enrichment of La is common in many samples, the conventional calculation ($Ce/Ce^* = 2 \times Ce_{(SN)} / [La_{(SN)} + Pr_{(SN)}]$, where $_{SN}$ refers to normalization of concentrations against PAAS) would result in apparent negative or false Ce anomalies (Bau and Dulski, 1996; Lawrence et al., 2006). Therefore, we calculate Ce anomalies using the equation $Ce/Ce^* = Ce_{(SN)} / [Pr_{(SN)}^2 / Nd_{(SN)}]$ as suggested by Lawrence et al. (2006). Other parameters, including Y/Ho, Eu/Eu^* [$= Eu_{(SN)} / (0.66Sm_{(SN)} + 0.33Tb_{(SN)})$] and Y/Y^* [$= 2Y_{(SN)} / (Dy_{(SN)} + Ho_{(SN)})$] are also given (Table 4).

The Doushantuo phosphorites at Weng'an have variable REE concentration ranging from 198 to 846 ppm with an average of 388 ppm (n = 17), and can be categorized into two groups (I, II). PAAS-normalized patterns for all samples, however, are highly consistent, as characterized by a hat-shape pattern with elevated MREE, relatively depleted

LREE and HREE, and relative enrichment of Y (Fig. 7a). The Y/Ho ratios range from 36.37 to 41.67, with an average of 38.64. The Eu/Eu* values range from 0.83 to 1.21, without an evident Eu anomaly. All samples lack a negative Ce anomaly (Fig. 7a), with Ce/Ce* values varying between 0.98 and 1.12 (Table 4). There is a clear decrease in ∑REE (total REE concentration) upsection from > 500 ppm for group I (samples 10-14) to < 350 ppm for group II (samples 15-19 and 23-29), whereas no clear stratigraphic trend for Ce/Ce* is observed although slight variations is present (Fig. 7b).

5. Discussion

5.1. Sedimentary and diagenetic evolution

Based on the above petrographic observations, a reconstruction can be attempted of the sedimentary and diagenetic evolution of the glaucony-bearing sandstone and phosphorites in the lower Doushantuo Formation. The following stages are hereby proposed:

1) Formation of authigenic (pristine) apatite. These are represented by the phosphatic flasers in the glauconitized sandstones (Fig. 2a, c-d). They show anastomosing fabrics, resembling microbial mats deposited *in situ* on the seafloor. The common presence of phosphatic intraclasts in the sandstone implies the wide presence of these phosphatic flasers, which must have been largely reworked later and deposited along with terrigenous detritus. In the Doushantuo Formation at Kaiyang, 50 km to the west of Weng'an, laminated phosphatic marl has also been observed and interpreted as a pristine phosphorite facies where apatite precipitated authigenically in sediments (Zhang et al., 2019).

2) Deposition of terrigenous clasts and phosphorite intraclasts. During the initial stage of the lower Doushantuo Formation, relatively high rates of terrigenous input lead to the deposition of sandstones, with subordinate reworked phosphatic intraclasts. With the transgression, terrigenous input decreases whereas phosphatic intraclasts gradually dominate the grains, resulting in the formation of granular phosphorites.

3) Authigenesis and early cementation and replacement. Penecontemporaneous cementation of the clasts by authigenic glaucony took place near the sediment/water

interface where both ferric and ferrous iron were available. An earlier generation of sulfides likely resulted from microbial sulfate reduction around organic debris in the microbial mat. Meanwhile, detrital quartz, feldspar, muscovite grains and phosphate intraclasts were partly replaced by glaucony.

4) Diagenetic transformation and replacement. These include recrystallization and overgrowth of sulfides, transformation of glaucony to other clay minerals (e.g., illite), and later replacement of phosphatic grains and glaucony by dolomite.

5.2. Origin and chemical evolution of the Doushantuo glaucony

Odin and Matter (1981) catergorized glaucony into four types based on the K_2O content: (1) the nascent (2 – 4 wt% K_2O), (2) the slightly evolved (4 – 6 wt% K_2O), (3) the evolved (6 – 8 wt% K_2O), and (4) the highly evolved (> 8 wt% K_2O). The Doushantuo glaucony is characterized by high K_2O (mostly > 8 wt%), consistent with the highly evolved type. This is supported by the poorly developed $(11\overline{2})$ reflection and the absence of (112) reflection in the XRD spectrum which are similar to evoled to highly evolved glaucony containing ca. 10% expandable layers (Odin and Matter, 1981). The lamellar and platy habit observed by SEM (Fig. 3d) further corroborates the 'highly evolved nature' (Odin and Matter 1981; Wigley and Compton 2007).

Three hypotheses have been proposed to explain the chemical evolution of authigenic glaucony (Fig. 6a): 1) The 'layer lattice theory' (Burst, 1958; Hower, 1961), which invokes the simultaneous incorporation of K and Fe into degraded layer silicates for the formation of glaucony; 2) The 'verdissement theory' (Odin and Matter, 1981), which considers initial precipitation of glauconitic smectite within micropores of the substrate followed by subsequent maturation by the incorporation of K into the glaucony structure without the increase of TFe_2O_3; and 3) The 'pseudomorphic replacement theory' (Dasgupta et al., 1990; Banerjee et al., 2008; Banerjee et al., 2016b), which emphasizes the supply of K and silica (Si) into porewater through dissolution of K-feldspars and quartz in substrates that facilitates glaucony authigenesis. The Doushantuo glaucony shows systematically high K_2O and variable TFe_2O_3, consistent with the trend predicted by the 'pseudomorphic replacement theory', like most Precambrian glaucony (Fig. 6a). This is supported by

petrographic observations that show partial replacement of K-feldspar, quartz and muscovite grains by glaucony (Fig. 2d, f-h; 3a-b).

It should be noted, however, the Doushantuo glaucony primarily occurs as interstitial cement, and thus more likely resulted from *in situ* authigenesis in the pore space. Dissolution of feldspar and mica during diagenesis was a major source K source for glauconitization in the Doushantuo Formation, whereas the dissolution of quartz grains likely supplied Si in the pore water environment. The high alkalinity of the Precambrian seawater and shallow porewater probably favored these processes (Banerjee et al., 2015). The SiO_2 content (avg. 57.6 wt%) in the Doushantuo glaucony is also comparable to that of Precambrian glaucony pellets (Ivanovskaya et al., 2006; Banerjee et al., 2008, 2015; Tang et al., 2017; Guimaraes al., 2000) but is higher than that of Phanerozoic evolved glaucony pellets (45.4 to 52.6 wt%, Odin and Matter, 1981), consistent with high Si concentrations in Precambrian oceans.

It is noted that type 2 (phosphorite-hosted) glaucony has systematically higher TFe_2O_3 content than type 1 (sandstone-hosted) (Fig. 6a), which likely results from the substitution of Al^{3+} by Fe^{3+} at the octahedral site as suggested in Fig. 6b. These kinds of cation substitution are common in minerals, leading to changes in crystal structure and small shifts of Raman peaks (e.g., Wang et al., 2001; Kuebler et al., 2006; Rividi et al., 2010). Specifically, following increase of the Fe content in solid solution micas, the Raman peaks show a systematic position shift towards lower wavenumber, which is attributed to substitution of Al^{3+} by Fe^{3+} in the octahedral site that affects the $(Si_2O_5)^{2-}$ vibrational modes (Wang et al., 2015). The systematic downshifts of main Raman peaks from type 1 to type 2 glauconies (Fig. 5) thus confirm that Al^{3+} is substituted by Fe^{3+} along with the progressive incorporation of Fe during the growth and maturation of the Doushantuo glaucony. The upsection decrease in glaucony abundance and its final disappearance is interpreted as a result of a decrease in detrital input and Al availability since the formation of glauconite is ultimately dependent on the available Al ion amounts in the system (Meunier and Albani, 2007).

Potential Fe sources for glaucony include iron-bearing freshwater (Odin and Matter, 1981; Kozłowska and Maliszewska, 2015), hydrothermal fluids, Fe-rich detrital minerals

(e.g., iron oxides and biotite), or Fe-rich seawater. The upsection increase of TFe_2O_3 in glaucony from type 1 (sandstone-hosted) to type 2 (phosphorite-hosted) excludes Fe-rich detrital minerals as a main Fe source, because type 1 is associated with abundant terrigenous clasts whereas type 2 mainly occur with apatite. Considering the widespread ferruginous conditions in deep water environment during the Ediacaran (e.g., Li et al., 2010; 2015), seawater was likely a main source of Fe^{2+} for the formation of the Doushantuo glaucony.

5.3. Redox conditions for the lower Doushantuo Formation

To assess the redox conditions during phosphogenesis, we use REE + Y patterns as well as Ce anomalies recorded in the Doushantuo phosphorites as proxies. The REE + Y in phosphorites might be affected by (i) the geochemical processes in seawater and pore water, (ii) terrigenous detrital contamination, and (iii) later metamorphism and weathering. Considering the fact that our samples are all from fresh drill cores and targets for *in situ* LA-ICP-MS analyses are carefully selected, surface weathering is unlikely to have significantly affected the REE signatures of the Doushantuo phosphorites. This is supported by the generally high ∑REE, because REE will tend to be lost during weathering processes (Sheilds & Stille, 2001). High-temperature metamorphism is also unlikely to have affected the REE + Y patterns of the phosphatic grains because they commonly retain their original cryptocrystalline nature (She et al., 2013) and their peak metamorphic temperature was lower than 300 °C (She et al., 2016). Although low-temperature alteration is common in the Doushantuo Formation (Zhang et al., 2019), it mainly affects the interstitial phases rather than the phosphatic grains because the latter consist of densely packed apatite nanocrystals (She et al., 2013) and hence have very low permeability. The low Al_2O_3 content and the absence of a positive correlation between Al_2O_3 and ∑REE (Fig. 8a) indicate that detrital contributions to the REE + Y patterns of our samples are insignificant. This is also supported by the relatively high Y/Ho ratios and poor correlation between Th and Y/Ho ratio (Fig. 8b), because terrigenous detrital components typically have low Y/Ho ratios (~28; Bau, 1996) and high Th concentrations. In fact, shale bands interbedded in the Weng'an phosphorites have much lower ∑REE (81-146 ppm) and show

a distinct PAAS-like REE pattern (Chen et al., 2003). These exclude the possibility that the REE + Y features of Doushantuo phosphorites have been significantly affected by terrigenous detritus.

It has been shown that REE signatures of granular phosphorite primarily records variations in the local conditions of diagenesis, while diagenetic redox conditions may broadly reflect local bottom-water redox conditions (e.g., Shields and Stille, 2001). All the Doushantuo samples show nearly identical REE patterns characterized by a slight MREE enrichment with depletions of LREE and HREE (Fig. 7a). These concave-down patterns are consistent with bulk rock REE data of equivalent outcrop samples of the Doushantuo Formation at Weng'an, although the latter have much lower ∑REE (94 ppm in average, n = 48; Chen et al., 2003; Shields et al., 2004). The good correlation between ∑REE and $Pr_{(SN)}/Yb_{(SN)}$ (Fig. 8c) suggests that diagenetic REE uptake tends to increase both REE abundance and LREE/HREE fractionation. Group I phosphorites, which are more closely related to glaucony (Fig. 7b), must have experienced much stronger diagenetic REE uptake as a result of more intense Fe redox cycling in a slightly more oxidising condition. The slight shifts of $La_{(SN)}/Sm_{(SN)}$ and $La_{(SN)}/Yb_{(SN)}$ ratios from seawater composition (Fig. 8d) suggest that REE systematics was probably influenced, to a minor extent, by both crystal surface adsorption and bulk crystal substitution during early diagenesis (Reynard et al., 1999).

Negative Ce anomalies in authigenic sediments are commonly considered as an indicator of formation in an oxic environment, because Ce(III) is readily oxidized into less soluble Ce(IV) in modern oxic ocean systems and then scavenged by suspended particles that sink through the water column and accumulate in sediments (Sholkovitz et al., 1994; Bau and Dulski, 1996). The absence of a negative Ce anomaly suggests that the formation of the Doushantuo phosphorites may have occurred largely in suboxic or anoxic environments without significant preferential scavenging of Ce from the ambient water. Alternatively, the phosphorites originally could have had negative Ce anomalies but these signatures were disguised during early diagenetic alteration in anoxic conditions. However, diagenetic alteration of Ce anomaly signals is expected to result in various Ce features, including highly positive Ce anomalies (Shields and Stille, 2001). Except for three samples

that have slightly positive Ce / Ce* values (1.06-1.12), most Doushantuo phosphorites show highly consistent, near unity Ce / Ce* even at the micrometer scale, as shown by the *in situ* REE data in Table 4. This suggest insignificant preferential Ce remobilization relative to the neighbouring REE during diagenesis, although an original small negative Ce anomaly cannot be completely excluded.

Since both Fe^{2+} and Fe^{3+} are simultaneously required for glauconitization, glaucony preferably precipitates in suboxic environments around the Fe redoxcline where Fe^{2+} is partially oxidized to Fe^{3+} (Meunier and El Albani, 2007; Tang et al., 2017). In K- and Fe-rich, fully reducing environments (e.g., ferruginous conditions), formation of berthierine is favored, while oxic conditions may promote goethite precipitation (Velde, 1992). Therefore, the wide occurrence of glaucony in the lower Doushantuo Formation supports a generally suboxic early diagenetic environment, which was in active exchange with more oxygenated bottom seawater. In addition, slight variations of redox states in the porewater and bottom water would have promoted extensive glaucony authigenesis (Tang et al., 2017). These variations would not be captured by the phosphorite Ce signature as long as the environmental redox potential does not exceed the threshold for Ce (III) oxidation. Banerjee et al (2016b) have shown that slightly reducing conditions favour the origin of high-Fe glaucony, whereas glaucony formed in slightly oxidising conditions is depleted in Fe. Therefore, the higher Fe content in type 2 (phosphorite-hosted) glaucony than in type 1 (sandstone-hosted) glaucony appears to reflect less oxidising conditions for type 2 glaucony.

Collectively, mineralogical context and REE geochemistry suggest that the lower Doushantuo Formation likely formed on a suboxic seafloor with slight fluctuations in redox states of pore and bottom water. In contrast, the upper Doushantuo phosphorites at Weng'an contain much lower REE and exhibit a distinct negative cerium anomaly, which implies predominantly oxic conditions in local seawater as well as during both phosphogenesis and early diagenetic REE scavenging (Chen et al., 2003; Shields et al., 2004). Therefore, available phosphorite REE data document a transition from a generally suboxic environment to an oxic environment through the Doushantuo Formation.

5.4. Fe-redox driven phosphatisation and glauconitization

Shaffer (1986) first noted the presence of a phosphorus concentration gradient near the redoxcline in modern sediments in the Black Sea, and proposed the 'Fe-redox pump' model to explain the concentration of phosphorus in the pore water. Subsequent studies on modern marine and lacustrine sediments have demonstrated that Fe-redox pumping is a main driver for the cycling of phosphorus (Froelich et al., 1988; Heggie et al., 1990; Wheat et al.,1996; Algeo and Ingall, 2007; Jilbert and Slomp, 2013; Cosmidis et al., 2014). Fe-redox pumping is a cyclic mechanism that enriches pore water phosphate levels by first transporting phosphate to the seafloor through adsorption onto Fe-(oxyhydr)oxides, which, upon burial, are dissolved below the suboxic-anoxic boundary and liberate adsorbed phosphate to pore water. The escape of phosphate is prevented by re-adsorption of phosphate onto Fe-(oxyhydr)oxides just above this redox interface (Heggie et al., 1990; Nelson et al., 2010). In the Precambrian, it is expected that anoxic intermediate and bottom water would have prevented Fe-redox pumping from operating in deeper settings (Pafahl and Hiatt, 2012). In shallow water environments, however, Fe-redox mediated cycling of phosphorus is often invoked as a key mechanism during phosphogenesis (e.g., Crosby et al., 2014; She et al., 2014; Cui et al., 2016) although direct evidence is lacking.

The occurrence of glaucony in the Doushantuo Formation and its association with phosphate at both macroscopic and microscopic scales indicate phosphatisation and glauconitization near the anoxic-oxic boundary in the sediments. As discussed earlier, the oxygen concentration in the pore water was probably not high enough to cause preferential Ce remobilisation. However, the extensive presence of glaucony demonstrate that redox cycling of Fe was active during early diagenesis. As Ce (IV) has a redox potential close to Mn (IV), which is higher than Fe (III) (Algeo & Li, 2020), glaucony authigenesis in the lower Doushantuo Formation likely took place around the ferric iron reduction zone, and below the manganese reduction zone. Fe-redox pumping thus led to the concentration of phosphorus and REE, as supported by the coincident decreases in ∑REE and glaucony abundance (Fig. 7b). Possible reactions related to the formation of apatite-glaucony associations are expressed in the following equations (equations 2 and 3 not balanced because of ion substitutions):

$$8FeOOH.PO_4^{3-} + C_2H_3O_2^- + 15H^+ \rightarrow 8Fe^{2+} + 2HCO_3^- + 12H_2O + 8PO_4^{3-} \quad (1)$$

$$10Ca^{2+} + 6PO_4^{3-} + 2F^- + HCO_3^- \rightarrow 2[Ca_5(PO_4, CO_3)_3F] + OH^- \quad (2)$$

$$FeOOH + Fe^{2+} + KAlSi_3O_8 + Mg^{2+} + H^+ \rightarrow K\,(Fe^{3+}, Al, Mg, Fe^{2+})_2\,(Si, Al)_4O_{10}(OH)_2\,(\text{glaucony}) \quad (3)$$

It is also noted that sulfide is ubiquitously present in the Doushantuo phosphatic granules (Fig. 2; She et al., 2013; She et al., 2016; Cui et al., 2016), which suggests that the precursors of granules are enriched in both P and Fe. These precursors likely consist of apatite, glaucony and possibly also vivianite (a ferrous phosphate). Diagenetic transformation of glaucony to less Fe-rich clays such as illite might have liberated Fe^{2+}, which, when combined with HS^- produced by microbial sulfate reduction, led to the formation of diagenetic sulfides.

Authigenic glaucony precipitation in Phanerozoic and modern oceans takes place mostly in middle shelf to upper slope environments (200-300 m depth) with low depositional rate or sediment starvation (Odin and Matter, 1981; Banerjee et al., 2016b). In contrast, Precambrian glaucony is more common in stratigraphic successions deposited in shallower-water environments with variable depositional rates (Banerjee et al., 2016b), as also observed in the Doushantuo Formation. Typical Precambrian shallow-water glaucony include those in sandstones of the 1.0-Ga Bhalukona Formation (Banerjee et al., 2015), central India and those associated with stromatolites in the 1.44-Ga Tieling Formation, North China (Tang et al., 2017). This distinction between Phanerozoic and Precambrian sediments also applies to marine phosphorites, which are restricted to shallow water environments in the Precambrian but formed across the entire shelf in the Phanerozoic (Nelson et al., 2010; Pufahl and Hiatt, 2012; She et al., 2014; Cui et al., 2016). In South China, Ediacaran phosphorite deposits are mostly distributed in coastal areas to shallow shelf environments, including the inner and outer shelves near or above the chemocline (Fig. 1a), whereas no significant phosphorite bed has been reported from the intra-shelf and slope sections, which were deposited below the chemocline (Table 1; Jiang et al., 2011). This further demonstrates that phosphorus enrichment regulated by Fe-redox cycling was a prerequisite for massive accumulation of phosphate and that the apatite-glaucony association in Doushantuo is a direct result of Fe-redox driven authigenesis.

5.5 A model for phosphogenesis and glaucogenesis

Based on previous paleogeographic reconstructions, we propose a model to explain the formation and spatial distribution of phosphorite and glaucony during the early Doushantuo period (Fig. 9). Major phosphorite deposits are all formed in shallow water environments above or near the redoxcline because in these areas Fe-redox pumping of phosphorus could operate either in the water column or within the sediments. Glaucony formation mainly occurs on the seafloor just above the redoxcline where Fe^{2+} was more readily available because of the presence of deep ferruginous water below the redoxcline. Degradation of organic matter through ferric iron reduction and sulfate reduction leads to the release of Fe^{2+} and HS^{-}, as well as FeOOH-bound and organic-bound phosphorus to the pore water. Replacement of K-feldspar and other detrital phases begins with the incorporation of Fe^{2+} to form a precursor K-Al-Si-Fe phase. In such reducing conditions, pyrite could have formed around the organic matter.

With the increase of redox potential in the bottom and pore water, the ferrous iron was partially oxidized and Fe^{3+} was incorporated into the precursor K-Al-Si-Fe phase at the expense of Al. Meanwhile, concentration of phosphate and precipitation of apatite were probably pomoted by sulfide-oxidizing bacteria which are known to be able to metabolize polyphosphates and release orthophosphate into pore waters (Schulz & Schulz, 2005). With frequent, transient redox fluctuations, repeated cycles of these processes led to progressive addition of Fe^{2+} and Fe^{3+} that eventually resulted in the formation of glaucony. At Weng'an, Fe-redox cycling resulted in the concentration of phosphorus and Fe^{2+} just below the water/sediment interface, which in turn led to the precipitation of calcium phosphate. Subsequent reworking and winnowing produced intraclasts of phosphate. Early diagenetic formation of glaucony is favored by fluctuations of the redoxcline, which facilitated the incorporation of both ferric and ferrous Fe (Fig. 9).

The occurrence of the Doushantuo apatite-glaucony association supports previous recognition of the tempo-spatial distribution of phosphorites (Nelson et al., 2010; Pufahl and Hiatt, 2012) and glaucony (Banerjee et al., 2015) that characterizes distinct environments of phosphogenesis and glaucogenesis in the Precambrian and Phanerozoic. It should be noted that although glaucony is abundant in Phanerozoic sedimentary

successions, it is relatively rare in the Precambrian (Banerjee et al., 2016b), probably due to post-depositional alteration to chlorite (Bansal et al., 2020) or surface weathering. Further investigations of the mineralogical relationships between phosphorite and glaucony (or its alteration products) in Precambrian successions hold great potential to further understanding of the paleoredox conditions of past seawater.

6. Conclusions

The lower Doushantuo Formation at Weng'an begins with terrigenous clastic deposition in shallow water peritidal environments, followed by a transgression that led to a decrease of detrital input and increase of intraclasts. Pristine phosphorite formed as phosphatic flasers in glauconitic sandstones and were subsequently reworked and redeposited, whereas glaucony occur as authigenic cement between detrital minerals and phosphate grains and as partial replacement of K-feldspar, quartz, muscovite and phosphate grains.

The Doushantuo glaucony is characterized by high K_2O but low and variable TFe_2O_3 contents, similar to other Precambrian glaucony. The compositional variability and Raman spectral features support the formation of glaucony by progressive incorporation of Fe into the mineral lattice, including Fe^{3+} substitution for Al^{3+}. Early diagenetic glaucony cementation occurred in suboxic pore water just below the sediment-water interface where both ferric and ferrous Fe were available and incorporation of iron into glaucony was probably promoted near the redoxcline where deep ferruginous water provided Fe^{2+}.

The phosphate grains exhibit consistent concave-down REE + Y patterns and do not show a negative Ce anomaly, which suggests the formation of pristine phosphorites in suboxic environments without significant preferential remobilisation of Ce during early diagenesis. The tempo-spatial distribution of glaucony and phosphorite in the lower Doushantuo Formation demonstrates the presence of a shallow redoxcline during the early Doushantuo Period. Phosphorus and Fe^{2+} were concentrated in anoxic bottom water and pore water by repeated cycles of oxidation and reduction of Fe-bearing phases and organic matter. Apatite-glaucony association is an indication of suboxic early diagenetic environments and can be a reliable mineralogical proxy, which, when present, to decipher shallow-water redox conditions in the Precambrian.

Acknowledgments

This work was financially supported by the Strategic Priority Research Program of Chinese Academy of Sciences (grant No. XDB26020102), National Natural Science Foundation of China (grant# 41825019, 41821001, 41272038), and the State Key Laboratory of Biogeology and Environmental Geology, China University of Geosciences (grant# GBL11801). Z.S. thanks Qun Chen and Chao Deng for their help in field work and acknowledges support from the Bureau of Geology and Mineral Resources of Guizhou Province for access to their core library. A. M. thanks Chengyuan Wang for assistance in data processing and Zihu Zhang for XRD analysis. We thank two anonymous reviewers for their constructive and helpful comments, and editor Frances Westall for her thoughtful handling of the manuscript.

References

Algeo, T.J., Ingall, E., 2007. Sedimentary C_{org} : P ratios, paleocean ventilation, and Phanerozoic atmospheric pO_2. Palaeogeogr. Palaeoclimatol. Palaeoecol. 256, 130–155.

Algeo, T.J., Li, C., 2020. Redox classification and calibration of redox thresholds in sedimentary systems. Geochim. Cosmochim. Acta (in press).

Amorosi, A., 1997. Detecting compositional, spatial, and temporal attributes of glaucony : a tool for provenance research. Sediment. Geol. 109, 135-153.

Amorosi, A., Sammartino, I., Tateo, F., 2007. Evolution patterns of glaucony maturity : A mineralogical and geochemical approach. Deep-Sea Research. II. Top. Stud. Oceanogr. 54, 1364–1374.

Bailey, S.W., 1980. Summary of recommendations of the AIPEA nomenclature committee. Clay Miner. 15, 85–93.

Bailey, J.V., Joye, S.B., Kalanetra, K.M., Flood, B.E. and Corsetti, F.A., 2007. Evidence of giant sulphur bacteria in Neoproterozoic phosphorites. Nature, 445: 198-201.

Banerjee, S., Bansal, U., Pande, K., Meena, S.S., 2016a. Compositional variability of glauconites within the Upper Cretaceous Karai Shale Formation, Cauvery Basin, India: Implications for evaluation of stratigraphic condensation. Sediment. Geol. 331, 12–29.

Banerjee, S., Bansal, U., Vilas Thorat, A., 2016b. A review on palaeogeographic implications and temporal variation in glaucony composition. J. Palaeogeogr. 5, 43–71.

Banerjee, S., Chattoraj, S.L., Saraswati, P.K., Dasgupta, S., Sarkar, U., 2012a. Substrate control on

formation and maturation of glauconites in the Middle Eocene Harudi Formation, western Kutch, India. Marine Petrol. Geol. 30, 144–160.

Banerjee, S., Chattoraj, S.L., Saraswati, P.K., Dasgupta, S., Sarkar, U., Bumby, A., 2012b. The origin and maturation of lagoonal glauconites: A case study from the Oligocene Maniyara Fort Formation, western Kutch, India. Geol. J. 47, 357–371.

Banerjee, S., Jeevankumar, S., Eriksson, P.G., 2008. Mg-rich ferric illite in marine transgressive and highstand systems tracts: Examples from the Paleoproterozoic Semri Group, central India. Precambrian Res. 162, 212–226.

Banerjee, S., Mondal, S., Chakraborty, P.P., Meena, S.S., 2015. Distinctive compositional characteristics and evolutionary trend of Precambrian glaucony: Example from Bhalukona Formation, Chhattisgarh basin, India. Precambrian Res. 271, 33–48.

Barfod, G.H., Albarède, F., Knoll, A.H., Xiao, S., Télouk, P., Frei, R., Baker, J., 2002. New Lu-Hf and Pb-Pb age constraints on the earliest animal fossils. Earth Planet. Sci. Lett. 201, 203–212.

Bansal, U., Banerjee, S., Nagendra, R., 2020. Is the rarity of glauconite in Precambrian Bhima Basin in India related to its chloritization? Precambrian Res. 336, 105509.

Bau, M., 1996. Controls on the fractionation of isovalent trace elements in magmatic and aqueous systems: Evidence from Y/Ho, Zr/Hf, and lanthanide tetrad effect. Contrib. Mineral. Petrol. 123, 323–333.

Bau, M., Dulski, P., 1996. Distribution of yttrium and rare-earth elements in the Penge and Kuruman iron-formations, Transvaal Supergroup, South Africa. Precambrian Res. 79, 37–55.

Brasier, M.D., 1980. The Lower Cambrian transgress ion and glauconite- phosphatic facies in Western Europe. J. Geol. Soc. Lond. 137, 695–703.

Burnett, W.C., 1980. Apatite-glauconite associations off Peru and Chile: palaeo-oceanographic implications. J. Geol. Soc. Lond. 137, 757–764.

Burst, J.F., 1958. “Glauconite” pellets: their mineral nature and applications to stratigraphic interpretations. Bull. Am. Assoc. Petrol. Geol. 42, 310–327.

Chafetz, H.S., Reid, A., 2000. Syndepositional shallow-water precipitation of glauconitic minerals. Sediment. Geol. 136, 29–42.

Chattoraj, S.L., Banerjee, S., Saraswati, P.K., 2009. Glauconites from the Late Palaeocene - Early Eocene Naredi Formation, western Kutch and their genetic implications. J. Geol. Soc. India 73, 567–574.

Chen, D.F., Dong, W.Q., Qi, L., Chen, G.Q., Chen, X.P., 2003. Possible REE constraints on the depositional and diagenetic environment of Doushantuo Formation phosphorites containing the

earliest metazoan fauna. Chem. Geol. 201, 103–118.

Chen, D.F., Dong, W.Q., Zhu, B.Q., Chen, X.P., 2004. Pb-Pb ages of Neoproterozoic Doushantuo phosphorites in South China: Constraints on early metazoan evolution and glaciation events. Precambrian Res. 132, 123–132.

Chen, G., Du, Y., Zhang, Y., Chen, Q., Fan, Y., Wang, Z. & Hua, T., 2015. Spatial and Temporal Variation and Mineralization Model of the Sinian Phosphorus-bearing Sequences in Central Guizhou Province. Geol. Sci. Techn. Info. 34(6), 17-25.

Chen, J., Algeo, T.J., Zhao, L., Chen, Z.Q., Cao, L., Zhang, L., Li, Y., 2015. Diagenetic uptake of rare earth elements by bioapatite, with an example from Lower Triassic conodonts of South China. Earth-Sci. Rev. 149, 181–202.

Chen, Y.Q., Jiang, S.Y., Ling, H.F., Yang, J.H., 2009. Pb-Pb dating of black shales from the Lower Cambrian and Neoproterozoic strata, South China. Chem. Erde-Geochem. 69, 183-189.

Condon, D., Zhu, M., Bowring, S., Wang, W., 2005. U-Pb Ages from the Neoproterozoic Doushantuo Formation, China. Science. 308, 95-98.

Cosmidis, J., Benzerara, K., Morin, G., Busigny, V., Lebeau, O., Jézéquel, D., Noël, V., Dublet, G., Othmane, G., 2014. Biomineralization of iron-phosphates in the water column of Lake Pavin (Massif Central, France). Geochim. Cosmochim. Acta 126, 78–96.

Crosby, C.H., Bailey, J.V., Sharma, M., 2014. Fossil evidence of iron-oxidizing chemolithotrophy linked to phosphogenesis in the wake of the Great Oxidation Event. Geology 42(11), 1015-1018.

Bailey, J.V., Joye, S.B., Kalanetra, K.M., Flood, B.E., Corsetti, F.A., 2007. Evidence of giant sulphur bacteria in Neoproterozoic phosphorites. Nature 445, 198-201.

Cui, H., Kaufman, A.J., Xiao, S., Zhu, M., Zhou, C., Liu, X.M., 2015. Redox architecture of an Ediacaran ocean margin: Integrated chemostratigraphic ($\delta^{13}C$-$\delta^{34}S$-$^{87}Sr/^{86}Sr$-Ce/Ce*) correlation of the Doushantuo Formation, South China. Chem. Geol. 405, 48–62.

Cui, H., Xiao, S., Zhou, C., Peng, Y., Kaufman, A.J., Plummer, R.E., 2016. Phosphogenesis associated with the Shuram Excursion: Petrographic and geochemical observations from the Ediacaran Doushantuo Formation of South China. Sediment. Geol. 341, 134–146.

Dasgupta, S., Chaudhuri, A.K., Fukuoka, M., 1990. Compositional Characteristics of Glauconitic Alterations of K-Feldspar from India and their Implications. J. Sediment. Petrol. 60, 277–287.

Deb, S.P., Fukuoka, M., 1998. Fe-Illites in a Proterozoic Deep Marine Slope Deposit in the Penganga Group of the Pranhita Godavari Valley: Their Origin and Environmental Significance. J. Geol. 106, 741–749.

Drits, V.A., Ivanovskaya, T.A., Sakharov, B.A., Zvyagina, B.B., Derkowski, A., Gor'kova, N.V., Pokrovskaya, E.V., Savichev, A.T., Zaitseva, T.S., 2010. Nature of the structural and crystal-chemical heterogeneity of the Mg-rich glauconite (Riphean, Anabar Uplift). Lithol. Miner. Resour. 45, 555–576.

El Albani, A., Meunier, A., Fursich, F., 2005. Unusual occurrence of glauconite in a shallow lagoonal environment. Terra Nova 17, 537–544.

Fan, H., Wen, H., Han, T., Zhu, X., Feng, L., Chang, H., 2018. Oceanic redox condition during the late Ediacaran (551–541 Ma), South China. Geochim. Cosmochim. Acta 238, 343–356.

Föllmi, K.B., 2016. Sedimentary condensation. Earth-Sci. Rev. 152, 143–180.

Froelich, P.N., Arthur, M.A., Burnett, W.C., Deakin, M., Hensley, V., Jahnke, R., Kaul, L., Kim, K.H., Roe, K., Soutar, A., Vathakanon, C., 1988. Early diagenesis of organic matter in Peru continental margin sediments: Phosphorite precipitation. Mar. Geol. 80, 309–343.

Giresse, P., Wiewio, A., 2001. Stratigraphic condensed deposition and diagenetic evolution of green clay minerals in deep water sediments on the Ivory Coast – Ghana Ridge. Mar. Geol. 179, 51-70.

Guimaraes, E.M., Velde, B., Hillier, S., Nicot, E., 2000. Diagenetic/anchimetamorphic changes on the Proterozoic glauconite and glaucony from the Paranoa Group, Midwestern Brazil. Rev. Bras. Geocie. 30, 363–366.

Heggie, D.T., Skyring, G.W., O'Brien, G.W., Reimers, C., Herczeg, A., Moriarty, D.J.W., Burnett, W.C., Milnes, A.R., 1990. Organic carbon cycling and modern phosphorite formation on the East Australian continental margin: An overview. Geol. Soc. Spec. Publ. 52, 87–117.

Hiatt, E.E., Pufahl, P.K., Edwards, C.T., 2015. Sedimentary phosphate and associated fossil bacteria in a Paleoproterozoic tidal flat in the 1.85 Ga Michigamme Formation. Sediment. Geol. 319, 24–39.

Hower, J., 1961. Some factors concerning the nature and origin of glauconite. Am. Mineral. 46, 313–334.

Huang, J., Feng, L., Chu, X., Sun, T., Wen, H., Qin, L., Shen, Y., 2017. A predominantly ferruginous condition in the Ediacaran deep ocean: Geochemistry of black shales in the Ediacaran Doushantuo Formation, South China. Precambrian Res. 295, 12–23.

Ivanovskaya, T.A., Gor'kova, N. V., Karpova, G. V., Pokrovskaya, E. V., 2006. Phyllosilicates (glauconite, illite, and chlorite) in terrigenous sediments of the Arymas Formation (Olenek High). Lithol. Miner. Resour. 41, 547–569.

Jarrar, G., Amireh, B., Zachmann, D., 2000. The major, trace and rare earth element geochemistry of glauconites from the early Cretaceous Kurnub Group of Jordan. Geochem. J. 34, 207–222.

Jiang, G., Shi, X., Zhang, S., Wang, Y., Xiao, S., 2011. Stratigraphy and paleogeography of the Ediacaran Doushantuo Formation (ca. 635 – 551 Ma) in South China. Gondwana Res. 19, 831–849.

Jilbert, T., Slomp, C.P., 2013. Iron and manganese shuttles control the formation of authigenic phosphorus minerals in the euxinic basins of the Baltic Sea. Geochim. Cosmochim. Acta 107, 155–169.

Kozłowska, A., Maliszewska, A., 2015. Berthierine in the Middle Jurassic sideritic rocks from southern Poland. Geol. Quart. 59, 551–564.

Kuebler, K.E., Jolliff, B.L., Wang, A., Haskin, L.A., 2006. Extracting olivine (Fo-Fa) compositions from Raman spectral peak positions. Geochim. Cosmochim. Acta. 70, 6201–6222.

Lawrence, M.G., Greig, A., Collerson, K.D., Kamber, B.S., 2006. Rare earth element and yttrium variability in South East Queensland waterways. Aquat. Geochem. 12, 39–72.

Lee, C.H., Choi, S.W., Suh, M., 2002. High iron glaucony from the continental shelf of the Yellow Sea off the southwestern Korean Peninsula. J. Asian Earth Sci. 20, 507–515.

Li, C., Love, G.D., Lyons, T.W., Fike, D.A., Sessions, A.L., Chu, X., 2010. A stratified redox model for the ediacaran ocean. Science. 328, 80–83.

Li, C., Planavsky, N.J., Shi, W., Zhang, Z., Zhou, C., Cheng, M., Tarhan, L.G., Luo, G., Xie, S., 2015. Ediacaran Marine Redox Heterogeneity and Early Animal Ecosystems. Sci. Rep. 5, 1–8.

Liu, Y., Hu, Z., Gao, S., Günther, D., Xu, J., Gao, C., Chen, H., 2008. In situ analysis of major and trace elements of anhydrous minerals by LA-ICP-MS without applying an internal standard. Chem. Geol. 257, 34–43.

Lyons, T.W., Severmann, S., 2006. A critical look at iron paleoredox proxies, New insights from modern euxinic marine basins. Geochim. Cosmochim. Acta 70, 5698-5722.

Lyons, T.W., Reinhard, C.T., Planavsky, N.J., 2014. The rise of oxygen in Earth's early ocean and atmosphere. Nature 506, 307–315.

McFadden, K.A., Huang, J., Chu, X., Jiang, G., Kaufman, A.J., Zhou, C., Yuan, X., Xiao, S., 2008. Pulsed oxidation and biological evolution in the Ediacaran Doushantuo Formation. Proc. Natl. Acad. Sci. U. S. A. 105, 3197–3202.

McLennan, S.M., 1989. Rare earth elements in sedimentary rocks: influence of provenance and sedimentary processes. In: Lipin, B.R., McKay, G.A. Eds., Geochemistry and Mineralogy of Rare Earth Elements. Min. Soc. Am. Rev. Mineral. 21, 169–200.

Meunier, A., El Albani, A., 2007. The glauconite-Fe-illite-Fe-smectite problem: A critical review. Terra Nova 19, 95–104.

Mullins, H.T., Rasch, R.F., 1985. Sea-floor phosphorites along the central California continental margin. Econ. Geol. 80, 696–715.

Muscente, A.D., Hawkins, A.D., Xiao, S., 2015. Fossil preservation through phosphatization and silicification in the Ediacaran Doushantuo Formation (South China): A comparative synthesis. Palaeogeogr. Palaeoclimatol. Palaeoecol. 434, 46–62.

Nelson, G.J., Pufahl, P.K., Hiatt, E.E., 2010. Paleoceanographic constraints on Precambrian phosphorite accumulation, Baraga Group, Michigan, USA. Sediment. Geol. 1–13.

Och, L.M., Shields-Zhou, Graham A, 2012. The Neoproterozoic Oxygenation Event : Environmental perturbations and biogeochemical cycling. Earth-Sci. Rev. 110, 26–57.

Odin, G., Lamboy, 1988. Glaucony from the margin off northwestern Spain. In: Odin, G.S. (Ed.), Green Marine Clays. Developments in Sedimentology. 45, pp. 249–275.

Odin, G.S., Matter, A., 1981. De glauconiarum origine. Sedimentology 28, 611–641.

Papineau, D., 2010. Global biogeochemical changes at both ends of the Proterozoic: Insights from phosphorites. Astrobiology 10, 165–181.

Ospitali, F., Bersani, D., Lonardo, G. D., Lottici, P. P., 2008. 'Green earths': vibrational and elemental characterization of glauconites, celadonites and historical pigments. J. Raman Spectrosc. 39: 1066–1073.

Pouchou, J.L., Pichoir, F., 1991. Quantitative analysis of homogeneous or stratified microvolumes applying the model "PAP". In K.F.J. Heinrich and D.E. Newbury, Eds., Electron Probe Quantitation, 31–75. Plenum Press, New York.

Pufahl, P.K., Grimm, K.A., 2003. Coated phosphate grains: Proxy for physical, chemical, and ecological changes in seawater. Geology 31, 801–804.

Pufahl, P.K., Hiatt, E.E., 2012. Oxygenation of the Earth's atmosphere-ocean system: A review of physical and chemical sedimentologic responses. Mar. Pet. Geol. 32, 1–20.

Rao, V., Lamboyb, M., Dupeubleb, P.A., 1993. Verdine and other associated authigenic (glaucony, phosphate) facies from the surficial sediments of the southwestern continental margin of India. Mar. Geol. 111, 133–158.

Reynard, B., Lécuyer, C., Grandjean, P., 1999. Crystal-chemical controls on rare-earth element concentrations in fossil biogenic apatites and implications for paleoenvironmental reconstructions. Chem. Geol. 155, 233–241.

Rividi, N., Van Zuilen, M., Philippot, P., Ménez, B., Godard, G., Poidatz, E., 2010. Calibration of

carbonate composition using micro-raman analysis: application to planetary surface exploration. Astrobiology 10, 293–309.

Sahoo, S. K., Planavsky, N. J., Kendall, B., Wang, X., Shi, X., Scott, C., Anbar, A. D., Lyons, T. W., Jiang, G. 2012. Ocean oxygenation in the wake of the Marinoan glaciation. Nature 489, 546-549.Shaffer, G., 1986. Phosphate pumps and shuttles in the Black Sea. Nature 321, 515–5.

Sarkar, S., Choudhuri, A., Banerjee, S., Tom Van Loon, A.J., Bose, P.K., 2014. Seismic and non-seismic soft-sediment deformation structures in the Proterozoic Bhander Limestone, central India. Geologos 20, 89–103.

She, Z., Strother, P., McMahon, G., Nittler, L.R., Wang, J., Zhang, J., Sang, L., Ma, C., Papineau, D., 2013. Terminal Proterozoic cyanobacterial blooms and phosphogenesis documented by the Doushantuo granular phosphorites I: In situ micro-analysis of textures and composition. Precambrian Res. 235, 20–35.

She, Z., Strother, P., Papineau, D., 2014. Terminal Proterozoic cyanobacterial blooms and phosphogenesis documented by the Doushantuo granular phosphorites II : Microbial diversity and C isotopes. Precambrian Res. 251, 62–79.

She, Z.B., Zhang, Y.T., Liu, W., Song, J., Zhang, Y., Li, C., Strother, P., Papineau, D., 2016. New observations of Ambient Inclusion Trails (AITs) and pyrite framboids in the Ediacaran Doushantuo Formation, South China. Palaeogeogr. Palaeoclimatol. Palaeoecol. 461, 374–388.

Shields, G., Kimura, H., Yang, J., Gammon, P., 2004. Sulphur isotopic evolution of Neoproterozoic-Cambrian seawater: New francolite-bound sulphate δ34S data and a critical appraisal of the existing record. Chem. Geol. 204, 163–182.

Shields, G., Stille, P., Strauss, H., Joachimski, M.M., 2001. Diagenetic constraints on the use of cerium anomalies as palaeoseawater redox proxies; an isotopic and REE study of Cambrian phosphorites. Chem. Geol. 175, 29–48.

Sholkovitz, E.R., Landing, W.M., Lewis, B.L., 1994. Ocean particle chemistry: The fractionation of rare earth elements between suspended particles and seawater. Geochim. Cosmochim. Acta 58, 1567–1579.

Schulz, H.N., Schulz, H.D., 2005. Large sulfur bacteria and the formation of phosphorite. Science 307, 416–418.

Tang, D., Shi, X., Ma, J., Jiang, G., Zhou, X., Shi, Q., 2017. Formation of shallow-water glaucony in weakly oxygenated Precambrian ocean: An example from the Mesoproterozoic Tieling Formation in North China. Precambrian Res. 294, 214–229.

Tribovillard, N., Algeo, T.J., Lyons, T., Riboulleau, A., 2006. Trace metals as paleoredox and paleoproductivity proxies: An update. Chem. Geol. 232, 12-32.

Velde, B., 1992. Introduction to Clay Minerals: Chemistry, Origins, Uses and Environmental Significance. Chapman and Hall, London. 36, 229–231.

Vernhet, E., Heubeck, C., Zhu, M.Y., Zhang, J.M., 2007. Stratigraphic reconstruction of the Ediacaran Yangtze platform margin (Hunan province, China) using a large olistolith. Palaeogeogr. Palaeoclimatol. Palaeoecol. 254, 123-139.

Wheat, C.G, Feely, R.A, Mottl, M.J., 1996. Phosphate removal by oceanic hydrothermal processes: An update of the phosphorus budget in the oceans. Geochim. Cosmochim. Acta 19, 3593-3608.

Wang, A., Freeman, J.J., Jolliff, B.L., 2015. Understanding the Raman spectral features of phyllosilicates. J. Raman Spectrosc. 46, 829–845.

Wang, A., Jolliff, B.L., Haskin, L.A., Kuebler, K.E., Viskupic, K.M., 2001. Characterization and comparison of structural and compositional features of planetary quadrilateral pyroxenes by Raman spectroscopy. Am. Mineral. 86, 790–806.

Wang, L., Shi, X., Jiang, G., 2012. Pyrite morphology and redox fluctuations recorded in the Ediacaran Doushantuo Formation. Palaeogeogr. Palaeoclimatol. Palaeoecol. 333–334, 218–227.

Wigley, R., Compton, J.S., 2007. Oligocene to Holocene glauconite-phosphorite grains from the Head of the Cape Canyon on the western margin of South Africa. Deep-Sea Res. II 54, 1375–1395.

Xiao, S., McFadden, K.A., Peek, S., Kaufman, A.J., Zhou, C., Jiang, G., Hu, J., 2012. Integrated chemostratigraphy of the Doushantuo Formation at the northern Xiaofenghe section (Yangtze Gorges, South China) and its implication for Ediacaran stratigraphic correlation and ocean redox models. Precambrian Res. 192–195, 125–141.

Xiao, S., Zhang, Y., Knoll, A.H., 1998. Three-dimensional preservation of algae and animal embryos in a Neoproterozoic phosphorite. Nature 391, 553-558.

Xiao, S., Zhou, C., Liu, P., Wang, D.A.N., Yuan, X., 2014. Phosphatized acanthomorphic acritarchs and related microfossils from the ediacaran doushantuo formation at weng'an (South China) and their implications for biostratigraphic correlation. J. Paleontol. 88, 1–67.

Ye, L., Chen, Q., Zhao, D., Chen, Z., Liu, K., 1989. The Phosphorites of China. SciencePress, Beijing.

Zhang, Y., Pufahl, P.K., Du, Y., Chen, G., Liu, J., Chen, Q., Wang, Z., Yu, W., 2019. Economic phosphorite from the Ediacaran Doushantuo Formation, South China, and the Neoproterozoic-Cambrian Phosphogenic Event. Sediment. Geol. 388, 1–19.

Zhou, C., Brasier, M. D., Xue,Y., 2001. Three-dimensional phosphatic preservation of giant acritarchs from the terminal Proterozoic Doushantuo Formation in Guizhou and Hubei provinces, South China. Palaeontology 44, 1157–1178.

Zhou, C., Xie, G., McFadden, K., Xiao, S., Yuan, X., 2007. The diversification and extinction of Doushantuo-Pertatataka acritarchs in South China: causes and biostratigraphic significance. Geol. J. 42, 229-262.

Zhou, C., Li, X., Xiao, S., Lan, Z., Ouyang, Q., Guan, C., Chen, Z., 2017. A new SIMS zircon U–Pb date from the Ediacaran Doushantuo Formation: age constraint on the Weng'an. Geol. Mag. 154, 1193-1201.

Zhu, B., Jiang, S.Y., 2017. A LA-ICP-MS analysis of rare earth elements on phosphatic grains of the Ediacaran Doushantuo phosphorite at Weng'an, South China: implication for depositional conditions and diagenetic processes. Geol. Mag. 154(6), 1381-1397.

Zhu, M., Zhang, J., Yang, A., 2007. Integrated Ediacaran (Sinian) chronostratigraphy of South China. Palaeogeogr. Palaeoclimatol. Palaeoecol. 254, 7–61.

Algabri et al_Fig.1

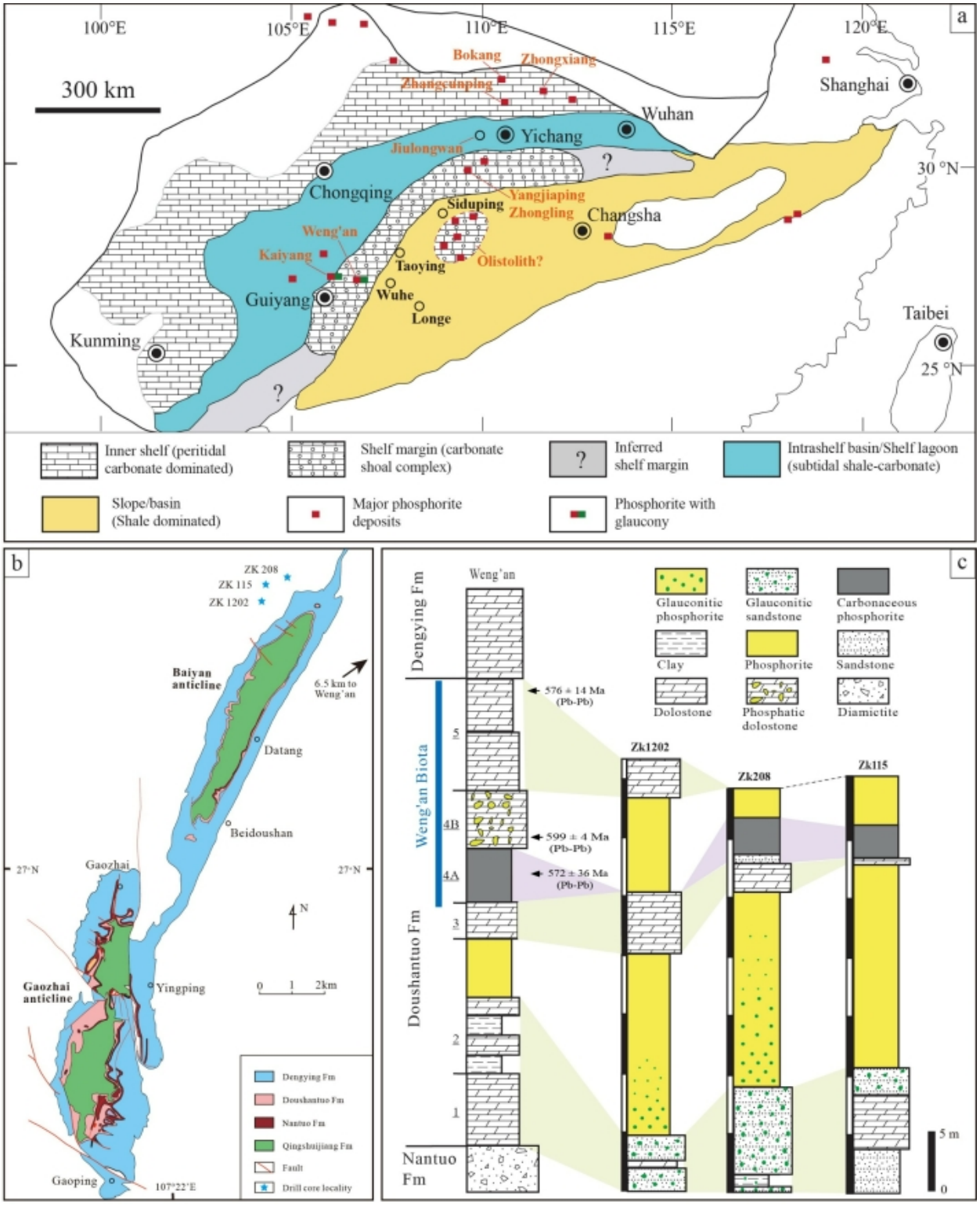

Fig. 1. Geological map and stratigraphic columns. a) A generalized paleogeographic map of the Yangtze Craton during the early Ediacaran Period (modified after Jiang et al., 2011), showing major phosphate deposits in the Doushantuo Formation (Ye et al., 1989) and a possible olistolith (Vernhet et al., 2007). b) A simplified geological map showing the Precambrian geology of the Baiyan - Gaozhai area with locations of studied drill holes. c) Stratigraphic columns of the studied drill cores (Zk1202, Zk208 and Zk115) of the Doushantuo Formation highlighting glaucony-bearing horizons. Note the upward decreasing trend of glaucony abundance. Age data are from Barford et al. (2002), Chen et al. (2004) and Chen et al. (2009).

Algabri et al_Fig.2

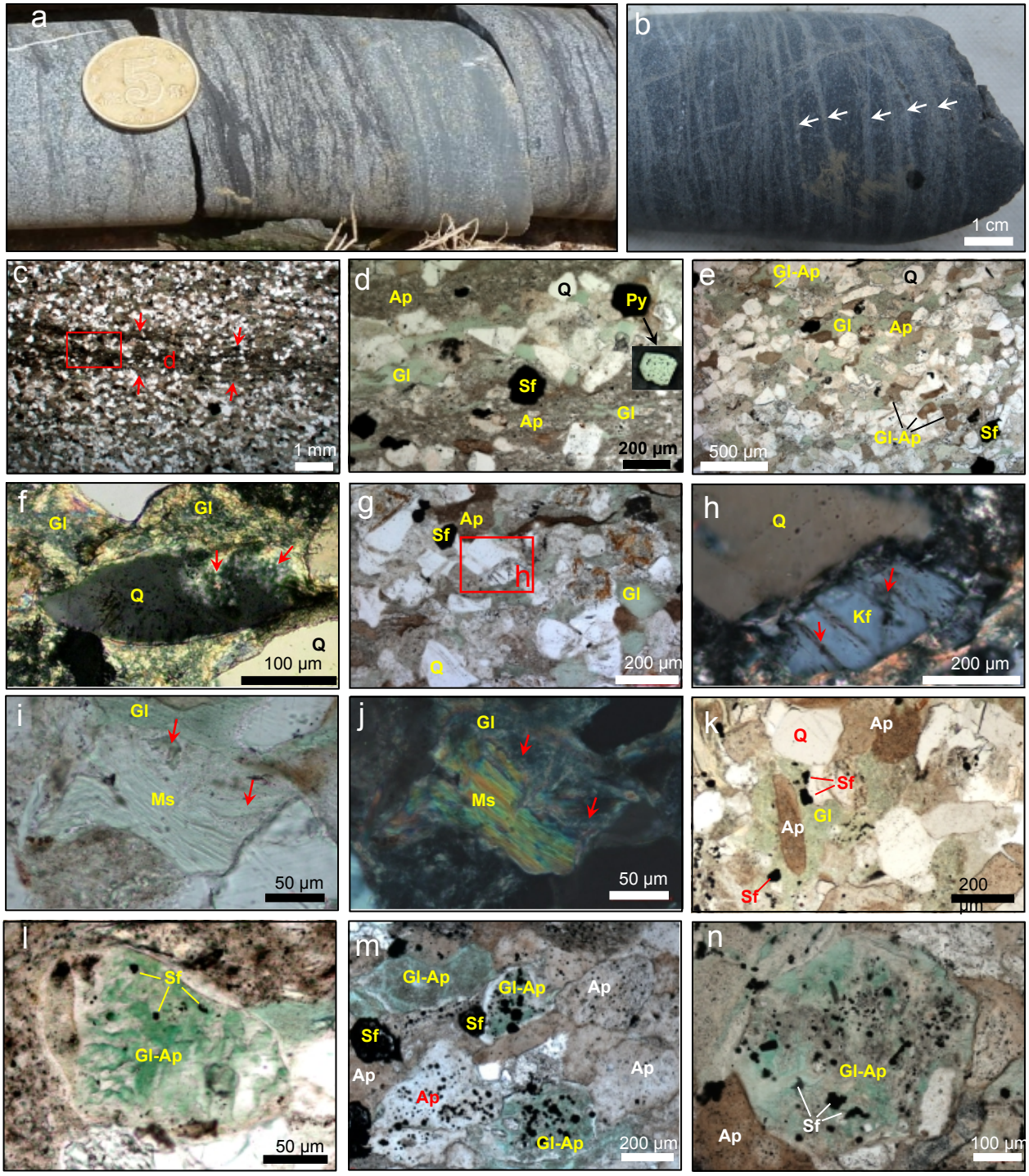

Fig. 2. Drill core photos (a-b) and photomicrographs (c-n) of glauconitic sandstones and phosphorites in the lower Doushantuo Formation. a) Glauconitic sandstone showing lenticular and flaser bedding. b) Granular phosphorite containing carbonate bands (arrows). c-j) Glauconitic sandstones consisting of detrital minerals, apatite grains and glaucony cement (type 1). c) Phosphatic flasers (arrows) in glauconitic sandstone. d) Magnified view of the flasers in (c) showing anastomosing structures with detrital grains embedded in a network of black-brownish apatite mass (inset, reflected light image of the pyrite grain). e) Glaucony cementing and replacing detrital quartz and phosphatic grains. f-g) Glaucony cementing partly replacing detrital quartz (f, arrows) and K-feldspar (g). h) Close-up of the K-feldspar partly replaced by glaucony (arrows) in (g). i-j) Glauconitized muscovite grain (arrows). k-n) Phosphorite containing glaucony (type 2) and sulfides. k) Glaucony cementing apatite grains. l-n) Glauconitized apatite grains containing abundant sulfides. Mineral abbreviations: Gl, glaucony; Ap, apatite; Gl-Ap, glauconitized apatite grains; Q, quartz; Sf, sulfide; Ms, muscovite; Kf, K-feldspar. Coin for scale in (a) is 20.5 mm in diameter. c-e, g, i, k-n), plane polarized light mode; f, h, j), crossed polarizers mode.

Algabri et al_Fig. 3

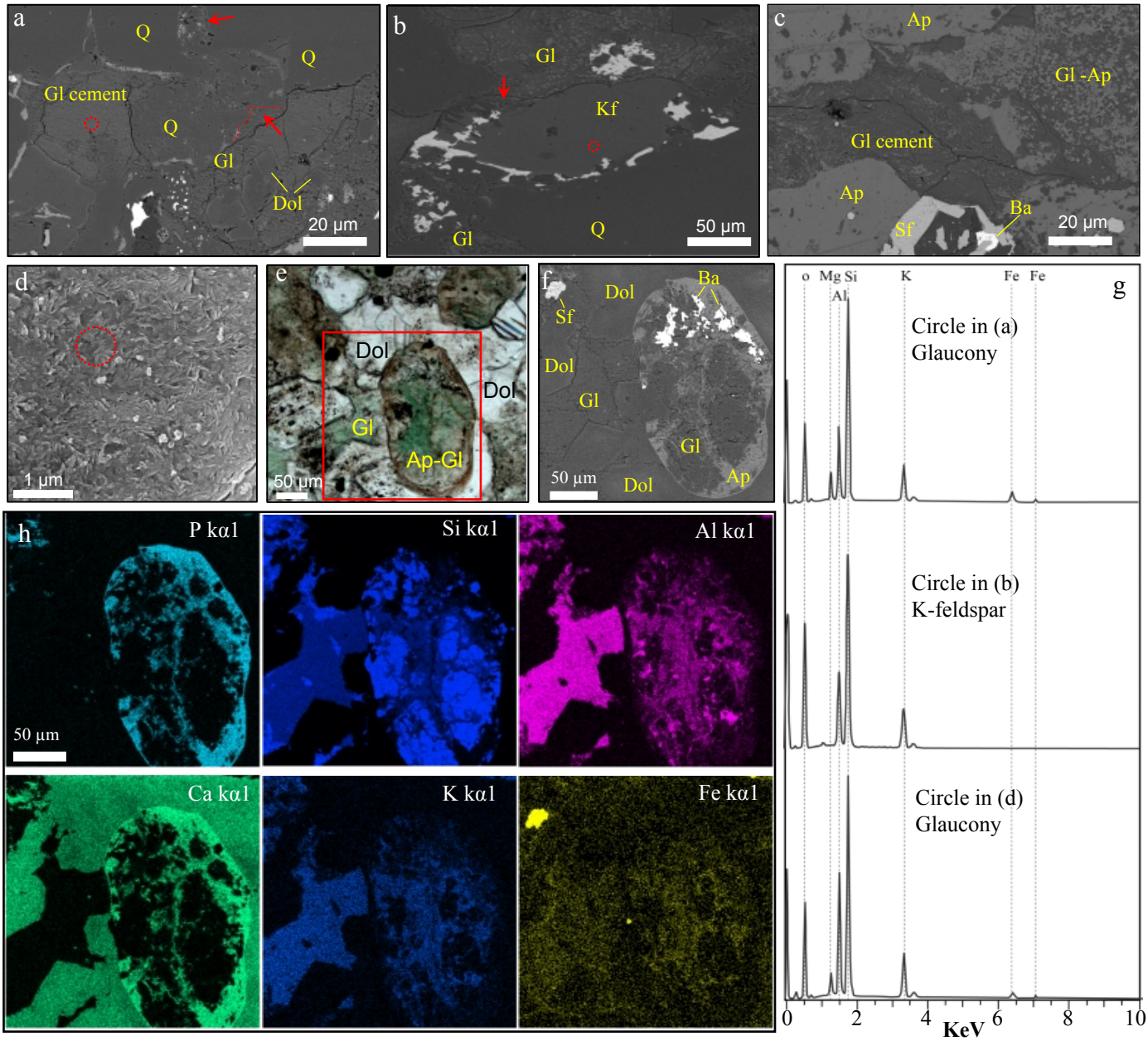

Fig. 3. SEM images (a-d, f), energy dispersive spectrometer (EDS) spectra (g) and elemental maps (h) of the Doushantuo glaucony and associated minerals. a) BSE image showing type 1 glaucony (Gl) occurring as cements as well as partly replacing detrital quartz grains (arrows). b) BSE image of a K-feldspar partly replaced by glaucony (arrow). c) BSE image showing type 2 glaucony, glauconitized apatite grain, sulfide and barite. d) High magnification secondary electron image of type 2 glaucony showing lamellar structure. e) Transmitted light image showing an apatite-glaucony grain and glaucony cement that were selected for EDS mapping. f) BSE image of the area outlined in (e). g) EDS spectra of the spots marked in (a), (b) and (d). h) EDS elemental maps of (f). Mineral abbreviations: Q, quartz; Ap, apatite; Gl, glaucony; Kf, K-feldspar; Sf, sulfide; Ba, barite.

Algabri et al_Fig. 4

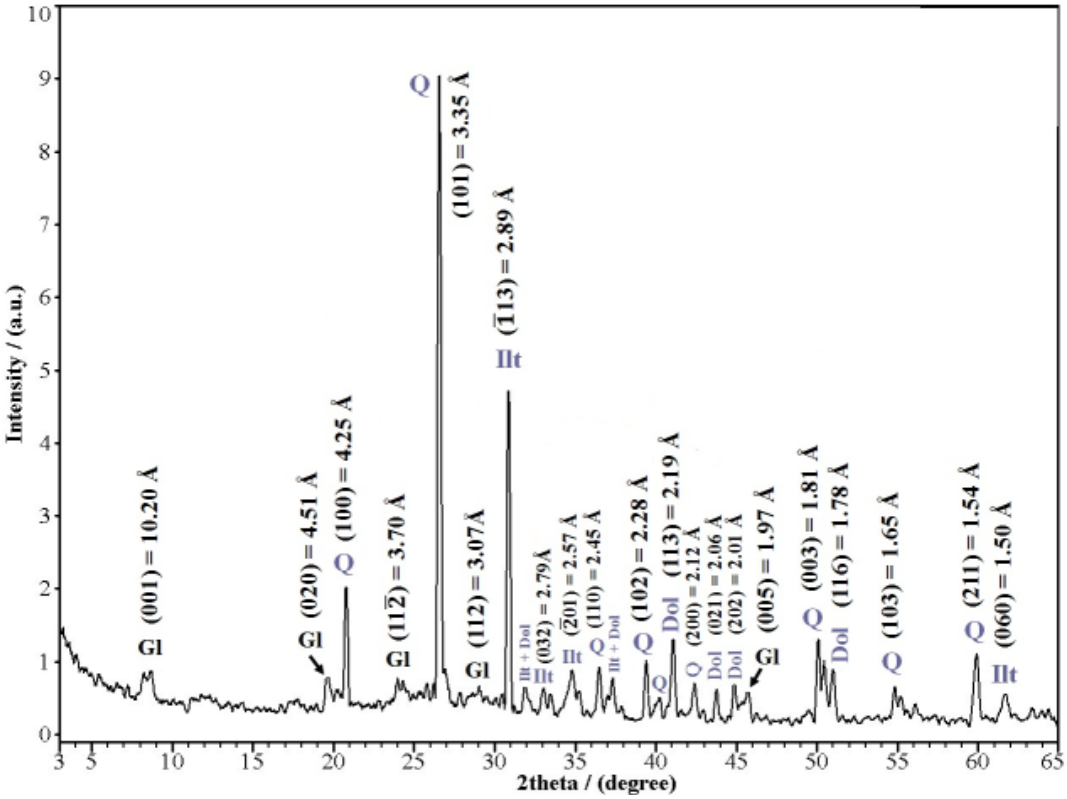

Fig. 4. XRD spectrum for a glauconitic sandstone (Zk1202-4). The diffraction peaks shown include those of glauconite (Gl), illite (Ilt), quartz (Q), dolomite (Dol) and their mixtures.

Algabri et al_Fig. 5

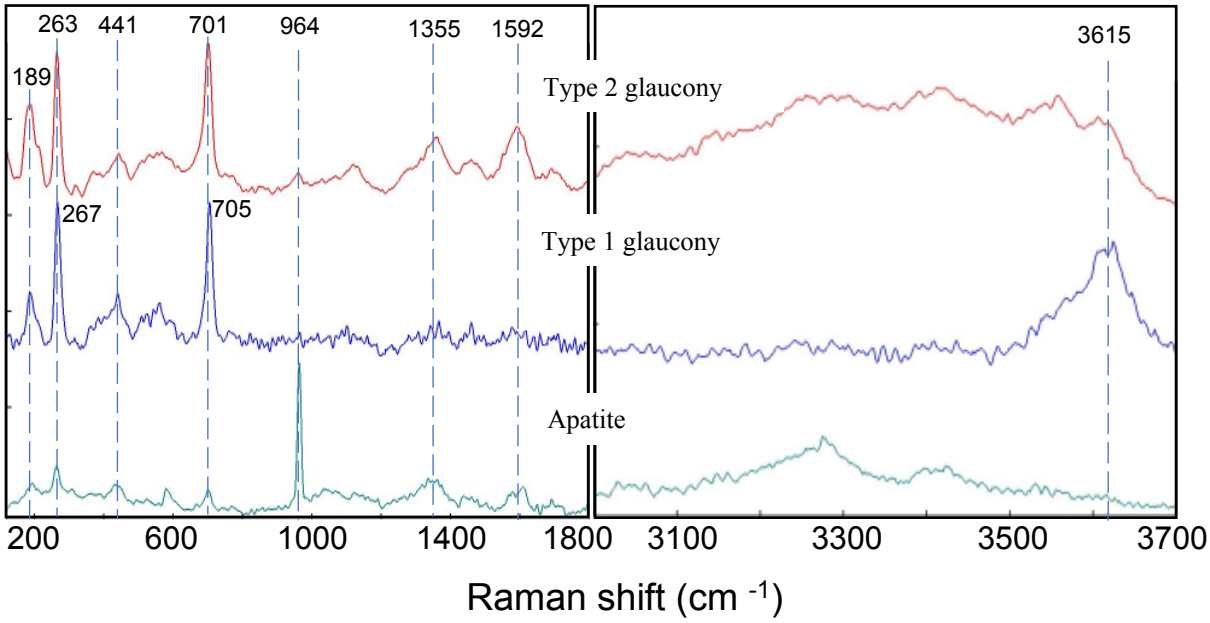

Fig. 5. Raman spectra of the Doushantuo glaucony and apatite.

Algabri et al_Fig. 6

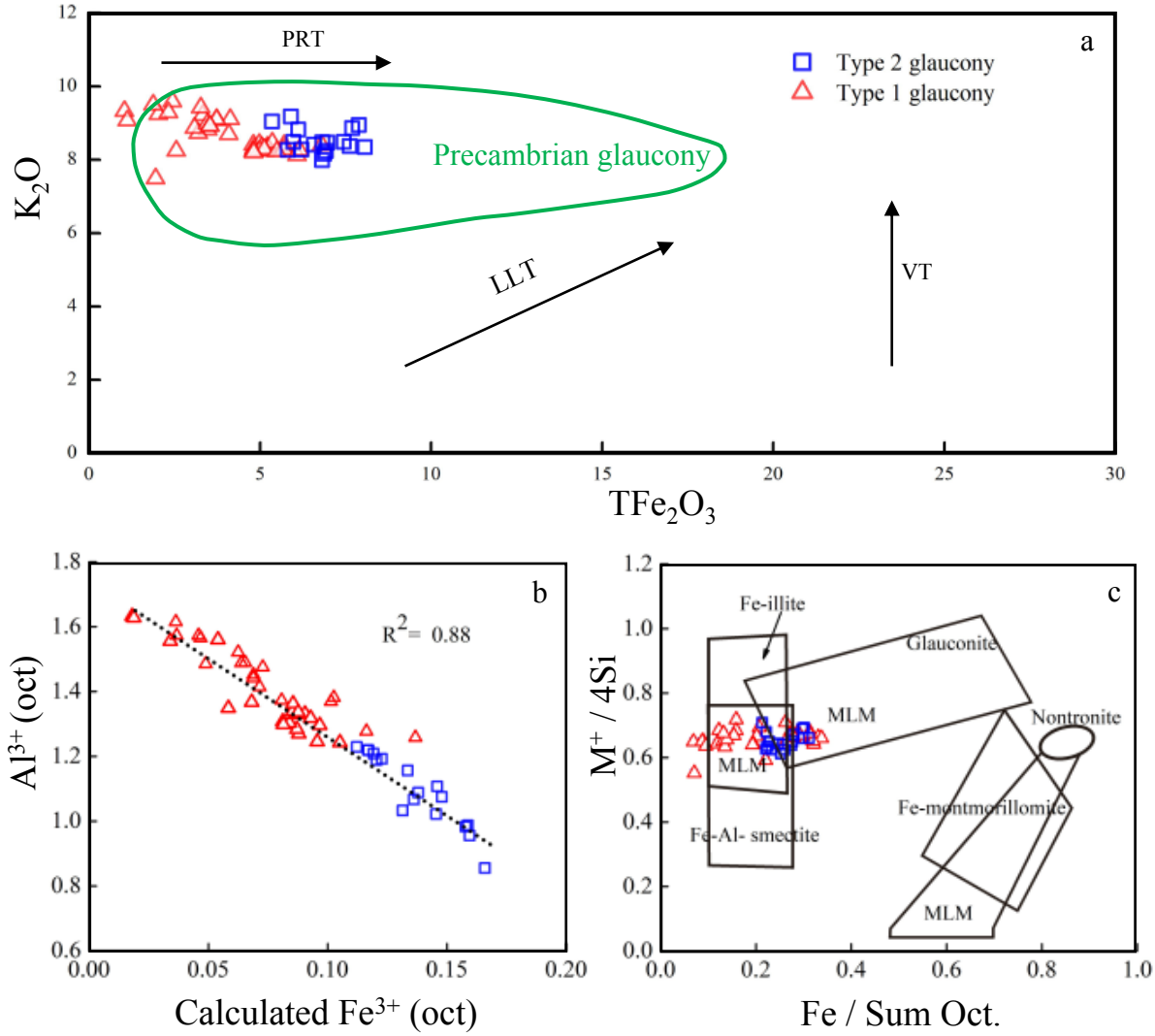

Fig. 6. Chemical composition of the two types of glaucony in the Doushantuo Formation. (a) Cross plot of K_2O vs. calculated TFe_2O_3, showing constantly high K_2O but variable TFe_2O_3 contents. Also shown is the compositional field of typical Precambrian glaucony (Banerjee et al., 2016b; Tang et al., 2017). Arrows indicate evolutionary trends of glaucony predicted by three hypotheses: the 'layer lattice theory' (LLT), the 'verdissement theory' (VT), and the "pseudomorphic replacement theory" (PRT). The K_2O - Fe_2O_3 relationship of most Phanerozoic glaucony closely follows the LLT and VT trends and are not presented here (cf. Banerjee et al., 2016b). (b) Diagram for Al^{3+} vs Fe^{3+} (calculated) in octahedral site for the Doushantuo Formation showing negative correlation. Note that the overall increase in Fe^{3+} from type 1 to type 2 glauconies at the expense of Al^{3+}. (c) Cross plot of Fe/Sum of octahedral charges vs (M^+/4Si) (M = interlayered cations, after Meunier and El Albani, 2007). Note that type 1 and 2 glauconies plots into the fields of glauconite, Fe-illite and Fe-Al smectite. MLM, Mixed layer minerals.

Algabri et al_Fig. 7

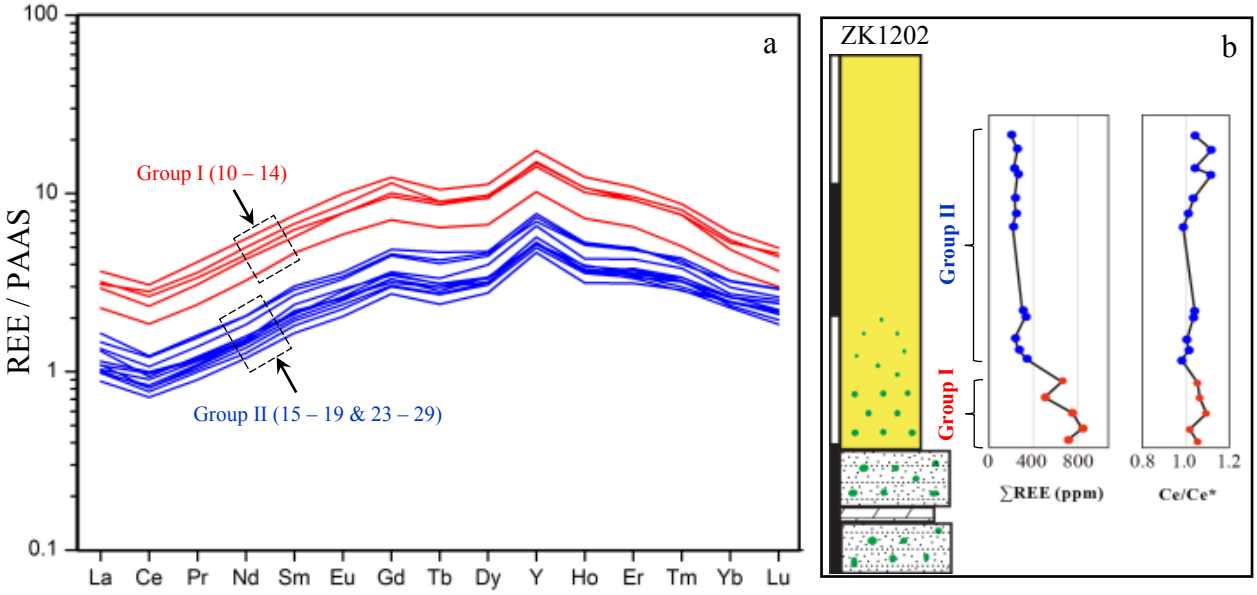

Fig. 7. Post-Archean Australian Shale (PAAS) -normalized REE + Y patterns (a) and stratigraphic variations of ∑REE and Ce/Ce* (b) for the Doushantuo phosphorites. Every spectrum in (a) represents the average composition of two to four spots on the same polished slab analyzed with LA-ICPMS. Note the roughly coincident decreases in ∑REE and glaucony abundance (shown by the green dots).

Algabri et al_Fig. 8

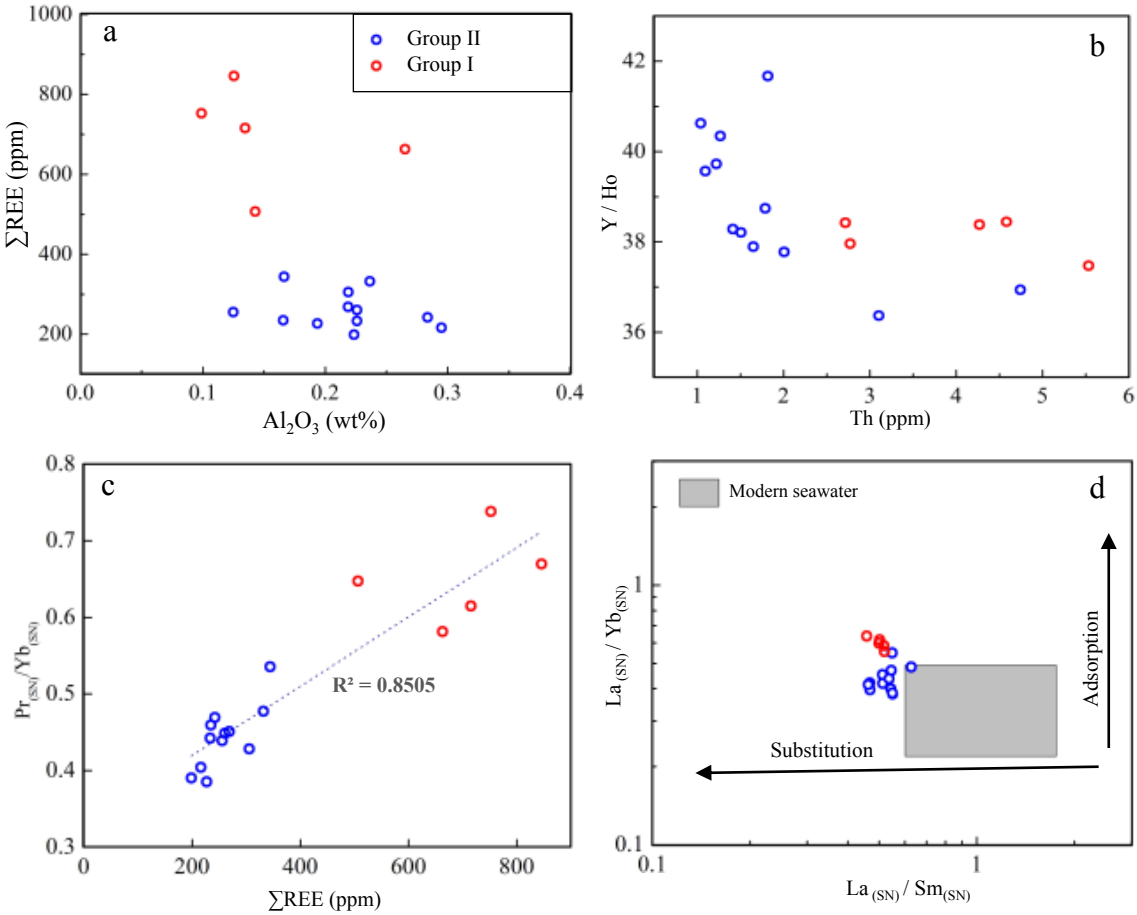

Fig. 8. Cross plots of Al_2O_3, Th and various REE parameters. Compositional range of modern oceanic water in (d) is from Reynard et al. (1999).

Algabri et al_Fig. 9

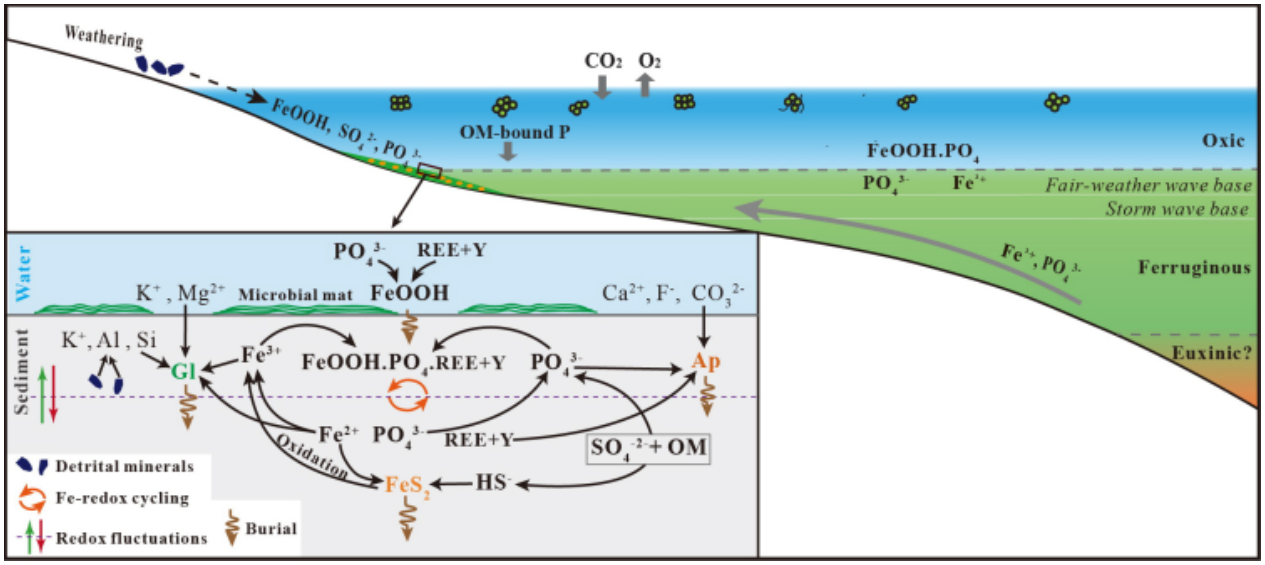

Fig. 9. Conceptual diagram of Fe redox cycling, glauconitization and phosphatisation processes for the lower Doushantuo Formation based on paleogeographic reconstructions and ocean chemistry models (Li et al., 2010; She et al., 2014; Muscente et al., 2015; Cui et al., 2016). In the peritidal environment near the redoxcline, Fe-redox processes at or below the sediment/water interface controlled the formation of glaucony (Gl) and apatite (Ap). Following deposition from the oxic seawater, Fe oxyhydroxides are dissolved in anoxic pore waters and Fe^{2+} and PO_4^{3-} are released. The reduced iron (Fe^{2+}) is refluxed back towards the sediment-water interface where it is incorporated into glaucony or again be oxidized and adsorb additional phosphate from oxygenated bottom waters, leading to the concentration of phosphate. Episodes of seawater oxygenation leads to redox variation in pore water and facilitate glaucony formation.

Table 1 Occurrence of glaucony and phosphorite in the Doushantuo Formation, South China

Depositional environment	Section	Locality	Glaucony abundance	Phosphate abundance	Reference
Shore*	Weng'an	Central Guizhou	Abundant	Abundant	This study; Zhou et al (2001); Zhu et al.(2007); Jiang et al (2011); Xiao et al (2014); Muscente et al (2015); Zhu and Jiang (2017)
	Kaiyang	Central Guizhou	Abundant	Abundant	Chen et al. (2015); Zhang et al (2019)
Inner shelf	Xiaofenghe	Western Hubei	None reported	Moderate	Zhu et al (2007); Xiao et al (2012); Muscente et al (2015); Cui et al (2016)
	Baokang	Western Hubei	None reported	Abundant	Zhou et al (2001); Xiao et al (2012); Muscente et al (2015); Cui et al (2016); She et al (2016)
	Zhangcunping	Western Hubei	None reported	Abundant	Zhu et al (2007); She et al (2013); Muscente et al (2015); Cui et al (2016)
Intra shelf	Jiulongwan	Western Hubei	None reported	Minor	McFadden et al (2008); Jiang et al (2011); Xiao et al (2012); Muscente et al (2015); Cui et al (2016)
Outer Shelf	Zhongling	Northwestern Hunan	None reported	Moderate	Zhu et al (2007); Li et al (2010); Jiang et al (2011); Cui et al (2015)
	Yangjiaping	Northwestern Hunan	None reported	Moderate	Zhu et al (2007); Jiang et al (2011); Cui et al (2015)
Slope	Siduping	Western Hunan	None reported	None reported	Jiang et al (2011)
	Taoying	Northeastern Guizhou	None reported	None reported	Jiang et al (2011)
	Wuhe	Southeastern Guizhou	None reported	None reported	Jiang et al (2011)
Basin	Longe	Southeastern Guizhou	None reported	None reported	Li et al (2010); Huang et al (2017)

* Sedimentary environment for Weng'an and Kaiyang have been alternatively interpreted as a shelf margin (Jiang et al., 2011).

Table 2 Quantitative EDS analysis results of oxide weight percentage and structural formula of glaucony in samples ZK1202-05 (type 1, spot No 1-18) and ZK1202-10 (type 2, spot No 19-35).

Spot No	MgO	Al_2O_3	SiO_2	K_2O	Cao	TFe_2O_3	Total	K^+	Na^+	Ca^{2+}	Fe^{2+}	Fe^{3+}	Mg^{2+}	Al^{3+} (oct)	Si^{+4}	Al^{+3} (tet)	R^{3+} (oct)	R^{3+} (tet)	Fe/Sum. Oct	$M^+/4Si$
1	4.0	22.3	52.6	8.2	0.0	4.8	91.9	0.72	0.00	0.00	0.10	0.14	0.40	1.38	3.59	0.41	1.53	0.41	0.17	0.64
2	5.4	22.0	61.3	8.3	0.0	6.2	103.1	0.64	0.00	0.00	0.12	0.16	0.49	1.28	3.71	0.29	1.44	0.29	0.20	0.59
3	4.1	21.8	54.1	8.2	0.0	4.8	92.9	0.70	0.00	0.00	0.10	0.14	0.41	1.37	3.64	0.36	1.51	0.36	0.17	0.64
4	4.1	26.0	56.6	9.2	0.0	3.3	99.2	0.74	0.00	0.00	0.07	0.09	0.38	1.49	3.56	0.44	1.58	0.44	0.11	0.66
5	4.0	28.9	57.1	9.6	0.0	2.5	102.0	0.75	0.00	0.00	0.05	0.07	0.37	1.57	3.49	0.51	1.63	0.51	0.08	0.65
6	3.7	29.5	56.0	9.5	0.0	1.9	100.5	0.75	0.00	0.00	0.04	0.05	0.34	1.62	3.46	0.54	1.67	0.54	0.06	0.65
7	3.8	28.1	55.3	9.3	0.0	2.3	98.9	0.75	0.00	0.00	0.05	0.06	0.36	1.57	3.48	0.52	1.64	0.52	0.08	0.65
8	3.8	26.3	54.3	8.9	0.0	3.1	96.3	0.73	0.00	0.00	0.06	0.09	0.37	1.52	3.52	0.48	1.61	0.48	0.11	0.64
9	3.3	24.3	64.2	7.5	0.0	2.0	101.2	0.57	0.00	0.00	0.04	0.05	0.29	1.57	3.86	0.14	1.62	0.14	0.06	0.55
10	4.6	24.9	56.4	9.0	0.0	3.5	98.4	0.73	0.00	0.00	0.07	0.10	0.44	1.44	3.58	0.42	1.54	0.42	0.12	0.65
11	5.2	25.4	58.9	9.1	0.0	3.8	102.3	0.71	0.00	0.00	0.07	0.10	0.47	1.41	3.59	0.41	1.51	0.41	0.12	0.63
12	3.6	24.9	58.8	9.4	0.0	3.3	100.0	0.75	0.00	0.00	0.06	0.09	0.33	1.49	3.66	0.34	1.58	0.34	0.11	0.68
13	4.7	22.9	59.2	9.1	0.0	4.1	100.0	0.72	0.00	0.00	0.08	0.11	0.44	1.37	3.69	0.31	1.49	0.31	0.14	0.67
14	3.8	25.2	58.2	9.1	0.0	3.7	100.0	0.72	0.00	0.00	0.07	0.10	0.35	1.48	3.63	0.37	1.58	0.37	0.12	0.66
15	4.0	24.7	58.4	8.9	0.5	3.5	99.5	0.71	0.00	0.03	0.07	0.10	0.37	1.45	3.64	0.36	1.55	0.36	0.12	0.68
16	3.2	21.2	64.8	8.2	0.0	2.6	100.0	0.64	0.00	0.00	0.05	0.07	0.29	1.49	3.96	0.04	1.55	0.04	0.09	0.64
17	4.0	22.3	55.5	8.4	1.6	6.8	93.8	0.69	0.00	0.11	0.14	0.19	0.38	1.26	3.57	0.43	1.45	0.43	0.23	0.71
18	4.0	24.7	58.4	8.9	0.5	3.5	100.1	0.71	0.00	0.03	0.07	0.10	0.37	1.45	3.64	0.36	1.55	0.36	0.12	0.68
Average	4.1	24.7	57.8	8.8	0.1	3.7	98.9	0.71	0.00	0.01	0.07	0.10	0.38	1.46	3.63	0.37	1.56	0.37	0.12	0.65
19	6.6	20.2	60.2	8.5	0.0	7.0	102.5	0.66	0.00	0.00	0.13	0.19	0.61	1.16	3.69	0.31	1.34	0.31	0.22	0.61
20	5.9	17.2	54.4	8.0	0.0	6.8	92.2	0.70	0.00	0.00	0.15	0.21	0.60	1.11	3.72	0.28	1.31	0.28	0.25	0.65
21	6.2	16.6	54.7	8.2	0.0	6.9	92.7	0.72	0.00	0.00	0.15	0.21	0.63	1.07	3.74	0.26	1.28	0.26	0.25	0.67
22	8.0	17.0	58.6	8.4	0.0	6.6	98.6	0.69	0.00	0.00	0.13	0.19	0.76	1.03	3.75	0.25	1.22	0.25	0.22	0.64
23	7.7	17.0	60.3	8.5	0.0	7.5	100.9	0.68	0.00	0.00	0.15	0.20	0.72	1.02	3.77	0.23	1.23	0.23	0.24	0.64
24	6.0	19.5	59.1	8.3	0.0	6.2	99.1	0.67	0.00	0.00	0.12	0.17	0.57	1.19	3.74	0.26	1.36	0.26	0.21	0.62
25	5.4	19.9	54.4	9.0	0.0	5.4	94.0	0.77	0.00	0.00	0.11	0.16	0.54	1.23	3.66	0.34	1.39	0.34	0.19	0.71
26	6.0	19.4	57.6	8.5	0.0	6.0	97.4	0.70	0.00	0.00	0.12	0.17	0.57	1.19	3.72	0.28	1.36	0.28	0.20	0.65

Spot No	MgO	Al_2O_3	SiO_2	K_2O	Cao	TFe_2O_3	Total	K^+	Na^+	Ca^{2+}	Fe^{2+}	Fe^{3+}	Mg^{2+}	Al^{3+} (oct)	Si^{+4}	Al^{+3} (tet)	R^{3+} (oct)	R^{3+} (tet)	Fe/Sum. Oct	$M^+/4Si$
27	5.8	20.9	57.8	9.2	0.0	5.9	99.6	0.74	0.00	0.00	0.12	0.16	0.55	1.22	3.66	0.34	1.38	0.34	0.20	0.68
28	7.0	17.9	58.2	8.2	0.0	6.9	98.1	0.67	0.00	0.00	0.14	0.19	0.67	1.09	3.73	0.27	1.28	0.27	0.23	0.62
29	7.4	18.0	58.2	8.5	0.0	6.8	98.9	0.69	0.00	0.00	0.14	0.19	0.71	1.07	3.71	0.29	1.26	0.29	0.23	0.64
30	7.7	15.8	57.9	9.0	0.0	7.9	98.3	0.74	0.00	0.00	0.16	0.22	0.75	0.96	3.75	0.25	1.18	0.25	0.27	0.69
31	7.4	16.3	55.7	8.4	0.0	7.6	95.4	0.71	0.00	0.00	0.16	0.22	0.74	0.99	3.71	0.29	1.21	0.29	0.27	0.66
32	6.4	21.6	58.0	8.8	0.0	6.1	101.0	0.70	0.00	0.00	0.12	0.17	0.60	1.21	3.62	0.38	1.38	0.38	0.20	0.64
33	7.4	16.3	56.8	8.9	0.0	7.7	97.0	0.74	0.00	0.00	0.16	0.22	0.72	0.98	3.72	0.28	1.21	0.28	0.26	0.69
34	9.0	14.0	57.3	8.3	0.0	8.1	96.7	0.70	0.00	0.00	0.17	0.23	0.88	0.85	3.77	0.23	1.09	0.23	0.28	0.66
35	5.9	20.2	57.1	8.3	0.0	5.8	97.3	0.68	0.00	0.00	0.12	0.16	0.57	1.22	3.68	0.32	1.38	0.32	0.20	0.63
Average	6.8	18.1	57.4	8.5	0.0	6.8	97.6	0.70	0.00	0.00	0.14	0.19	0.66	1.09	3.71	0.29	1.29	0.29	0.23	0.65

Note: R^{3+}, trivalent cations in tetrahedral (tet.) and octahedral (oct.) sites of glauconite; M^+, monovalent cations in interlayer sites of glauconite. An average value of $Fe^{2+}/\Sigma Fe$ of typical Precambrian glaucony (Banerjee et al., 2015; Tang et al., 2017) is used for the calculation of structural formula.

Table 3 EPMA analysis results of oxide weight percentage (wt%) and structural formula of glaucony in sample ZK1202-04 (type 1).

Spot No	SiO_2	Al_2O_3	TiO_2	TFe_2O_3	MgO	CaO	Na_2O	K_2O	Total	Na^+	Ca^{2+}	K^+	Fe^{2+}	Fe^{3+}	Mg^{2+}	Al^{3+} (oct)	Si^{4+}	Al^{3+} (tet)	R^{3+} (oct)	R^{3+} (tet)	Fe/Sum. Oct	$M^+/4Si$
1	54.0	26.3	0.1	2.0	3.5	0.1	0.1	9.2	95.4	0.01	0.01	0.77	0.04	0.06	0.35	1.56	3.53	0.47	1.61	0.47	0.23	0.69
2	55.0	22.3	0.1	3.5	5.3	0.2	0.1	8.8	95.2	0.01	0.01	0.74	0.07	0.10	0.51	1.35	3.62	0.38	1.45	0.38	0.35	0.68
3	52.4	26.9	0.1	3.2	3.0	0.1	0.1	8.7	94.6	0.02	0.02	0.73	0.07	0.09	0.30	1.56	3.46	0.54	1.65	0.54	0.24	0.67
4	55.7	22.6	0.1	4.1	4.5	0.3	0.1	8.7	96.0	0.01	0.01	0.72	0.08	0.12	0.43	1.37	3.63	0.37	1.48	0.37	0.33	0.68
5	55.4	21.1	0.1	4.8	4.8	0.3	0.1	8.4	94.8	0.01	0.01	0.71	0.10	0.14	0.47	1.31	3.66	0.34	1.45	0.34	0.37	0.66
6	55.8	20.4	0.1	5.2	4.9	0.2	0.1	8.4	95.1	0.01	0.01	0.70	0.11	0.15	0.48	1.27	3.68	0.32	1.42	0.32	0.39	0.66
7	56.4	20.1	0.1	5.7	4.9	0.3	0.1	8.4	95.9	0.01	0.01	0.70	0.12	0.16	0.48	1.25	3.70	0.30	1.41	0.30	0.40	0.66
8	56.5	20.8	0.1	5.2	4.8	0.3	0.0	8.3	96.1	0.00	0.00	0.69	0.11	0.15	0.47	1.28	3.69	0.31	1.43	0.31	0.38	0.64
9	55.4	21.2	0.1	5.0	4.7	0.2	0.0	8.4	95.1	0.00	0.00	0.71	0.10	0.14	0.47	1.30	3.65	0.35	1.45	0.35	0.38	0.66
10	55.6	21.0	0.1	4.8	4.8	0.3	0.1	8.3	95.0	0.01	0.01	0.70	0.10	0.14	0.48	1.30	3.67	0.33	1.44	0.33	0.38	0.65
11	55.7	18.5	0.0	6.1	4.0	0.4	0.1	8.1	92.9	0.01	0.01	0.70	0.13	0.18	0.40	1.24	3.77	0.23	1.42	0.23	0.39	0.68
12	56.3	20.7	0.0	5.4	3.6	0.3	0.0	8.5	94.8	0.00	0.00	0.71	0.11	0.16	0.36	1.33	3.72	0.28	1.49	0.28	0.34	0.67
13	56.4	19.8	0.0	5.7	3.8	0.3	0.1	8.3	94.4	0.01	0.01	0.70	0.12	0.17	0.38	1.30	3.75	0.25	1.46	0.25	0.36	0.67
14	52.9	26.1	0.0	1.1	2.7	0.1	0.0	9.3	92.3	0.00	0.00	0.80	0.02	0.03	0.28	1.63	3.56	0.44	1.66	0.44	0.17	0.72
15	55.6	26.2	0.0	1.1	2.8	0.1	0.0	9.1	95.0	0.00	0.00	0.75	0.02	0.03	0.27	1.63	3.62	0.38	1.66	0.38	0.17	0.68
16	55.7	19.9	0.1	5.1	3.6	0.2	0.1	8.3	93.0	0.01	0.01	0.72	0.11	0.15	0.36	1.33	3.75	0.25	1.48	0.25	0.33	0.68
17	55.9	20.2	0.0	5.0	3.6	0.2	0.1	8.2	93.2	0.01	0.01	0.70	0.10	0.15	0.36	1.34	3.75	0.25	1.49	0.25	0.33	0.67
18	57.4	21.2	0.0	5.1	3.6	0.2	0.0	8.2	95.8	0.01	0.01	0.68	0.10	0.15	0.35	1.36	3.74	0.26	1.51	0.26	0.32	0.65
19	55.8	20.2	0.1	5.1	3.5	0.3	0.0	8.3	93.4	0.00	0.00	0.71	0.11	0.15	0.35	1.34	3.74	0.26	1.49	0.26	0.33	0.67
20	56.7	20.0	0.1	5.5	3.7	0.3	0.0	8.2	94.5	0.01	0.01	0.69	0.11	0.16	0.36	1.32	3.76	0.24	1.48	0.24	0.34	0.66
Average	55.5	21.8	0.1	4.4	4.0	0.2	0.1	8.5	94.6	0.01	0.01	0.72	0.09	0.13	0.39	1.37	3.67	0.33	1.50	0.33	0.33	0.67

Table 4 Major element (wt%) and REE + Y concentrations (ppm) and calculated parameters for the ZK1202 phosphorites.

S.N.	MgO	Al_2O_3	P_2O_5	MnO	FeO	CaO	La	Ce	Pr	Nd	Sm	Eu	Gd	Tb	Dy	Ho	Er	Tm	Yb	Lu	Y	Th	∑REE	Y/Ho	Ce/Ce*	Eu/Eu*	$Pr_{(SN)}/Yb_{(SN)}$
18-01	0.17	0.01	42.56	0.05	0.20	53.01	50.84	81.60	11.68	57.56	13.08	2.99	16.87	2.87	17.79	4.52	12.44	1.71	8.65	1.20	171.87	3.43	283.80	38.00	1.00	0.99	0.43
18-02	0.26	0.34	40.68	0.06	0.69	52.64	52.36	87.60	12.17	65.92	14.23	3.51	20.32	2.88	18.79	4.83	12.71	1.43	8.62	1.21	171.25	4.70	306.60	35.40	1.13	1.11	0.45
18-03	0.14	0.25	39.13	0.04	0.17	53.46	56.62	102.49	15.03	76.76	18.93	3.68	23.11	3.47	25.12	5.37	14.20	1.90	8.80	1.29	196.53	4.25	356.80	36.60	1.01	0.91	0.55
18-04	0.19	0.34	39.19	0.10	0.35	55.05	64.20	111.95	15.74	77.63	18.08	4.60	24.90	3.87	24.97	5.62	15.64	1.98	10.45	1.38	212.14	6.59	381.00	37.70	1.01	1.12	0.48
18 avg.	0.19	0.24	40.39	0.06	0.35	53.54	56.00	95.91	13.66	69.47	16.08	3.70	21.30	3.27	21.67	5.09	13.75	1.75	9.13	1.27	187.95	4.74	332.05	36.94	1.03	1.00	0.48
19-01*	0.34	2.31	28.33	0.09	1.07	46.88	42.97	80.14	11.56	59.12	15.21	3.70	18.44	2.71	16.50	3.89	11.48	1.43	7.69	0.97	157.39	2.62	275.80	40.40	1.02	1.16	0.48
19-02	0.14	0.39	36.24	0.04	0.21	54.86	52.35	88.96	12.60	66.11	15.37	3.79	20.37	3.04	19.92	4.97	13.46	1.51	8.86	1.24	192.35	2.40	312.50	38.70	1.07	1.12	0.45
19-03	0.11	0.15	37.42	0.04	0.66	54.94	46.62	68.33	9.42	49.60	11.19	2.61	17.12	2.73	18.98	4.77	13.51	1.57	9.01	1.15	187.06	1.38	256.60	39.20	1.10	0.97	0.33
19-04	0.06	0.12	37.88	0.03	0.12	55.25	55.42	97.39	14.56	71.52	18.30	4.29	25.00	3.63	23.74	5.68	15.64	1.81	9.35	1.39	217.39	1.58	347.70	38.30	0.95	1.07	0.50
19 avg.	0.10	0.22	37.18	0.03	0.33	55.02	51.46	84.89	12.19	62.41	14.95	3.57	20.83	3.14	20.88	5.14	14.20	1.63	9.08	1.26	198.93	1.79	305.62	38.74	1.04	1.10	0.43
23-01*	0.16	0.60	37.94	0.03	0.22	55.05	38.46	61.82	8.87	42.11	9.57	2.36	13.46	2.05	13.89	3.26	9.87	1.29	6.86	0.94	126.45	2.34	214.80	38.80	0.96	1.09	0.41
23-02	0.14	0.30	37.83	0.05	0.17	57.26	41.43	63.93	9.22	43.61	10.93	2.49	14.36	2.14	15.59	3.75	9.90	1.36	7.50	0.90	142.92	1.04	227.10	38.10	0.95	1.04	0.39
23-03	0.16	0.19	37.25	0.04	0.19	57.83	37.27	67.57	9.28	46.91	10.84	2.79	14.48	2.15	13.87	3.74	9.62	1.27	6.69	1.05	131.19	2.28	227.50	35.10	1.06	1.17	0.44
23-04	0.11	0.09	36.35	0.06	0.11	59.29	33.29	52.80	7.85	39.40	8.97	2.08	13.62	2.06	14.21	3.41	9.21	1.26	6.80	0.95	135.02	0.94	195.90	39.60	0.98	0.99	0.37
23 avg.	0.14	0.29	37.34	0.04	0.17	57.36	37.61	61.53	8.80	43.00	10.08	2.43	13.98	2.10	14.39	3.54	9.65	1.29	6.96	0.96	133.90	1.65	216.34	37.89	0.99	1.10	0.40
24-01	0.12	0.30	41.15	0.03	0.13	54.53	43.21	79.30	10.85	52.83	13.41	2.93	16.60	2.39	15.94	3.88	10.47	1.21	7.13	0.99	144.66	2.76	261.10	37.30	1.03	1.04	0.49
24-02	0.13	0.32	40.50	0.03	0.16	54.87	36.44	64.34	9.68	45.17	11.04	2.50	14.97	2.03	15.16	3.52	9.17	1.05	6.67	0.82	134.78	1.43	222.60	38.30	0.90	1.06	0.46
24-03*	0.21	0.69	37.26	0.04	0.51	52.20	40.48	68.58	9.29	43.60	10.60	2.48	13.00	2.00	13.44	3.34	8.93	1.19	6.53	0.98	126.17	2.47	224.40	37.80	1.00	1.08	0.45
24-04	0.14	0.22	38.79	0.03	0.11	55.37	38.17	72.18	9.82	50.82	12.16	2.91	14.86	2.18	16.73	3.71	10.10	1.37	6.84	1.01	140.02	1.83	242.90	37.80	1.10	1.13	0.46
24 avg.	0.13	0.28	40.15	0.03	0.13	54.92	39.27	71.94	10.12	49.61	12.20	2.78	15.48	2.20	15.94	3.70	9.92	1.21	6.88	0.94	139.82	2.01	242.18	37.78	1.01	1.10	0.47
25-01	0.14	0.34	30.57	0.04	0.10	53.26	35.38	60.03	8.83	48.57	11.34	2.72	12.94	2.06	14.37	3.51	9.23	1.01	7.08	0.86	131.98	1.07	217.90	37.60	1.08	1.13	0.40
25-02*	0.16	0.70	33.57	0.06	0.28	55.43	35.19	59.06	8.80	42.88	9.57	2.70	13.63	2.05	13.55	3.15	9.51	1.22	6.58	0.89	130.08	1.39	208.80	41.30	0.95	1.24	0.43

* These data are excluded from the calculation of average (avg.) values.

Table 4 continued

S.N.	MgO	Al_2O_3	P_2O_5	MnO	FeO	CaO	La	Ce	Pr	Nd	Sm	Eu	Gd	Tb	Dy	Ho	Er	Tm	Yb	Lu	Y	Th	∑REE	Y/Ho	Ce/Ce*	Eu/Eu*	$Pr_{(SN)}/Yb_{(SN)}$
25-03	0.08	0.09	34.41	0.03	0.07	56.71	42.31	83.04	11.34	59.62	14.02	3.07	17.39	2.68	16.90	4.12	10.71	1.35	7.64	1.05	155.65	2.44	275.30	37.80	1.11	1.01	0.47
25-04	0.09	0.25	31.71	0.03	0.08	52.94	34.62	57.30	8.91	43.78	9.79	2.69	13.86	2.17	13.53	3.35	8.61	1.11	6.25	0.81	132.13	0.73	206.80	39.40	0.91	1.19	0.46
25 avg.	0.11	0.23	32.23	0.03	0.08	54.30	37.44	66.79	9.69	50.65	11.72	2.83	14.73	2.30	14.93	3.66	9.52	1.15	6.99	0.91	139.92	1.41	233.32	38.28	1.04	1.10	0.44
26-01*	0.28	0.92	34.02	0.08	0.91	55.47	35.50	59.62	7.86	38.89	9.94	2.15	11.82	1.87	13.28	2.80	8.86	1.14	6.49	0.84	115.41	4.98	201.00	41.20	1.08	1.00	0.39
26-02	0.20	0.22	36.84	0.05	0.35	56.95	38.68	62.37	8.77	44.55	9.93	2.33	13.89	2.08	13.68	3.36	8.99	1.24	6.36	0.98	129.62	1.80	217.20	38.60	1.04	1.04	0.44
26-03*	0.26	0.54	37.16	0.05	0.19	56.71	36.38	57.96	7.92	37.85	8.10	2.19	11.68	1.83	12.19	2.98	7.87	1.09	6.22	0.72	112.41	1.66	195.00	37.70	1.01	1.17	0.41
26-04	0.18	0.23	38.62	0.05	0.17	56.77	48.63	96.16	12.10	62.79	13.90	3.36	19.29	2.72	17.56	4.46	11.44	1.49	8.45	1.13	152.32	4.41	303.50	34.10	1.19	1.11	0.46
26 avg.	0.19	0.23	37.73	0.05	0.26	56.86	43.65	79.26	10.44	53.67	11.91	2.85	16.59	2.40	15.62	3.91	10.22	1.37	7.41	1.05	140.97	3.10	260.35	36.37	1.12	1.10	0.45
27-01	0.22	0.27	39.47	0.05	0.08	54.93	34.69	59.01	8.07	42.24	10.32	2.41	12.61	1.81	14.02	3.13	9.82	1.22	6.84	0.92	127.05	1.40	207.10	40.60	1.11	1.12	0.38
27-02	0.14	0.35	38.20	0.04	0.55	52.78	33.81	48.64	6.89	35.99	7.02	1.98	10.82	1.62	12.64	3.08	9.17	1.25	7.20	0.99	130.01	0.51	181.10	42.20	1.06	1.20	0.31
27-03	0.13	0.08	41.12	0.05	0.19	54.61	40.18	61.76	8.77	42.11	10.06	2.43	12.50	2.08	13.59	3.60	10.93	1.35	7.25	0.91	144.22	1.30	217.50	40.10	0.98	1.08	0.39
27-04	0.13	0.07	41.64	0.03	0.07	54.12	45.74	88.60	12.73	64.22	15.38	3.48	20.97	2.98	19.21	4.50	13.35	1.66	8.59	1.03	173.40	1.86	302.40	38.60	1.01	1.04	0.47
27 avg.	0.16	0.19	40.11	0.04	0.22	54.11	38.60	64.50	9.11	46.14	10.70	2.57	14.22	2.12	14.86	3.58	10.82	1.37	7.47	0.96	143.67	1.27	227.04	40.35	1.04	1.10	0.39
28-01	0.17	0.12	39.29	0.08	0.32	55.54	39.69	71.10	9.50	47.85	12.16	2.87	14.44	2.17	14.43	3.45	9.80	1.24	7.10	1.07	132.77	1.42	236.90	38.50	1.09	1.12	0.43
28-02*	0.31	2.36	36.08	0.13	0.51	50.24	39.45	74.99	9.53	48.80	12.31	2.73	14.85	2.14	14.20	3.42	9.40	1.28	6.98	0.87	131.98	1.42	241.00	38.60	1.16	1.06	0.44
28-03	0.14	0.17	42.80	0.07	0.32	53.13	49.50	102.79	13.11	66.12	17.38	4.18	21.23	3.15	20.14	4.66	12.14	1.51	8.02	1.06	167.15	2.00	325.00	35.90	1.14	1.14	0.52
28-04	0.09	0.08	44.25	0.04	0.44	52.24	35.04	59.35	7.98	41.29	10.17	2.39	12.82	1.94	13.05	3.10	8.46	1.16	6.92	1.00	124.55	1.10	204.70	40.20	1.11	1.09	0.37
28 avg.	0.13	0.12	42.12	0.06	0.36	53.64	41.41	77.75	10.20	51.75	13.24	3.15	16.17	2.42	15.87	3.73	10.13	1.30	7.35	1.04	141.49	1.51	255.51	38.21	1.11	1.10	0.44
29-01	0.12	0.19	42.83	0.02	0.16	52.60	37.97	66.15	9.09	45.94	11.01	2.63	14.19	2.18	14.43	3.26	9.54	1.30	7.03	0.85	133.33	1.08	225.60	40.90	1.06	1.09	0.41
29-02	0.07	0.14	41.56	0.03	0.14	52.66	33.25	53.84	7.60	38.23	8.94	2.15	12.05	1.95	13.29	3.29	9.08	1.26	6.89	0.93	133.38	0.85	192.80	40.50	1.03	1.05	0.35
29-03	0.14	0.31	38.28	0.10	0.27	50.77	25.15	36.17	5.31	24.86	5.67	1.24	8.77	1.21	8.12	2.24	7.09	0.87	5.28	0.66	97.42	0.58	132.60	43.50	0.92	0.97	0.32
29-04	0.10	0.26	36.11	0.03	0.11	51.83	38.56	73.04	9.84	52.32	10.91	2.81	16.00	2.06	15.88	3.71	10.12	1.24	6.62	0.76	139.41	1.65	243.90	37.60	1.14	1.20	0.47
29 avg.	0.11	0.22	39.70	0.04	0.17	51.96	33.73	57.30	7.96	40.34	9.13	2.21	12.75	1.85	12.93	3.12	8.96	1.17	6.45	0.80	125.89	1.04	198.70	40.63	1.04	1.10	0.39

* These data are excluded from the calculation of average (avg.) values.